The Evolution of Plume Fronts in the Rhine Region of Freshwater Influence

Rijnsburger, Sabine; Flores, Raúl P.; Pietrzak, Julie D.; Horner-Devine, Alexander R.; Souza, Alejandro J.; Zijl, Firmijn

DOI
10.1029/2019JC015927

Publication date
2021

Document Version
Final published version

Published in
Journal of Geophysical Research: Oceans

Citation (APA)
Rijnsburger, S., Flores, R. P., Pietrzak, J. D., Horner-Devine, A. R., Souza, A. J., & Zijl, F. (2021). The Evolution of Plume Fronts in the Rhine Region of Freshwater Influence. *Journal of Geophysical Research: Oceans*, *126*(7), 1-28. Article e2019JC015927. https://doi.org/10.1029/2019JC015927

JGR Oceans

RESEARCH ARTICLE
10.1029/2019JC015927

Special Section:
Contributions from the Physics of Estuaries and Coastal Seas meeting, 2018

The Evolution of Plume Fronts in the Rhine Region of Freshwater Influence

Sabine Rijnsburger[1], Raúl P. Flores[2,3], Julie D. Pietrzak[1], Alexander R. Horner-Devine[2], Alejandro J. Souza[4], and Firmijn Zijl[5]

[1]Department of Hydraulic Engineering, Delft University of Technology, Delft, The Netherlands, [2]Department of Civil and Environmental Engineering, University of Washington, Seattle, WA, USA, [3]Departamento de Obras Civiles, Universidad Tecnica Federico Santa Maria, Valparaiso, Chile, [4]CINVESTAV, Mérida, Yucatan, Mexico, [5]Deltares, Delft, The Netherlands

Abstract The Rhine region of freshwater influence (ROFI) is strongly stratified, rotational, relatively shallow and has large tides, resulting in a dynamic field of fronts that are formed by multiple processes. We use a 3D numerical model to obtain a conceptual picture of the frontal structure and the processes responsible for generating this multiple front structure in the Rhine ROFI. The horizontal salinity gradient and numerical tracers are used to identify three different types of fronts: outer, inner, tidal plume and relic tidal plume fronts. Tidal plume front (TPF) trajectories together with the tracers demonstrate that TPFs exist for longer than one tidal cycle. A Lagrangian frontogenesis analysis shows that the fronts are strengthened mainly as a result of increased convergence, which is observed to occur at times when tidal straining is large. Additionally the alongshore tidal excursion and the dominance of the tidal currents over the intrinsic frontal propagation speed, trap TPFs within 20 km from the river mouth. Trapping and re-strengthening maintain several fronts at a time in the mid-field region, resulting in a multi-frontal system. The observation of a complex river plume system is expected to be important for cross-shore exchange, transport and coastal ecology.

Plain Language Summary Rivers transport sediments, nutrients, and contaminants into the coastal ocean. A river plume is formed when the freshwater enters the ocean, where the edges of this river plume are the boundary between river and ocean water. These boundaries are called fronts and relate to large horizontal density gradients. These fronts are important for the transport of freshwater away from the river mouth. Our study shows that multiple fronts are observed in the Rhine region of freshwater influence. These multiple fronts result in a complex system. Our study unravels which processes are responsible for the presence of multiple fronts, which will change the overall dynamics in coastal areas influencing the transport of sediments, nutrients and contaminants.

Key Points:

- Tidal straining re-strengthens fronts hours after their initial formation
- Tidal advection leads to the trapping of tidal plume fronts, generating a multi-frontal system
- The persistence of Rhine plume fronts is due to convergence associated with bulk plume circulation

Supporting Information:

Supporting Information may be found in the online version of this article.

Correspondence to:

S. Rijnsburger,
s.rijnsburger@tudelft.nl

Citation:

Rijnsburger, S., Flores, R. P., Pietrzak, J. D., Horner-Devine, A. R., Souza, A. J., & Zijl, F. (2021). The evolution of plume fronts in the Rhine region of freshwater influence. *Journal of Geophysical Research: Oceans*, *126*, e2019JC015927. https://doi.org/10.1029/2019JC015927

Received 6 DEC 2019
Accepted 22 JUN 2021

1. Introduction

Oceanic fronts are strong lateral gradients of density forming a boundary between two different water masses (Cromwell & Reid, 1956). These fronts are associated with strong surface convergence resulting in downwelling, which leads to a clear surface signature in the form of foam with often floating debris and phytoplankton (Cromwell & Reid, 1956; Garvine & Monk, 1974). Fronts are observed on the boundaries and sometimes in the interior of river plumes, where they play an important role in the vertical and horizontal transport and mixing of river water with coastal waters (Hickey et al., 2010; Horner-Devine et al., 2015). The Rhine region of freshwater influence (ROFI), also known as the Rhine River plume, includes multiple fronts that persist for more than one tidal cycle from the river mouth to 15–20 km downstream, and play an important role in mixing and transport processes (Flores et al., 2017; Horner-Devine et al., 2017; Rijnsburger et al., 2018a). The understanding of frontal dynamics and their impact on the environment is important for coastal regions vulnerable to sea level rise and coastal erosion, such as the Dutch coast (Kabat et al., 2009; Nicholls & Cazenave, 2010). In this work we describe the dynamics of the fronts observed in the Rhine ROFI, classifying their different generation mechanisms and examining the processes by which they are maintained or weakened.

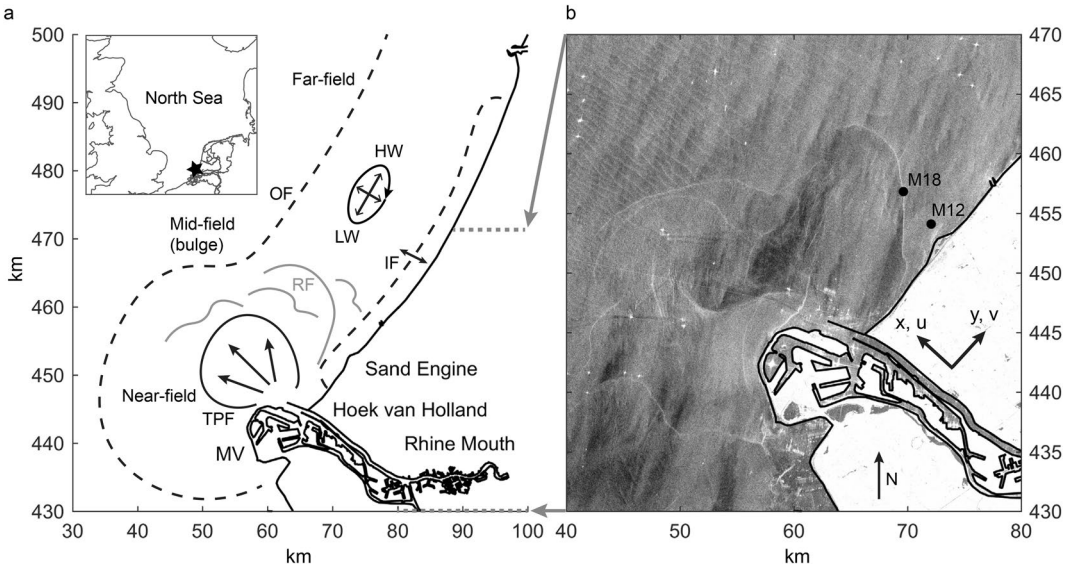

Figure 1. Schematic of different river plume fronts and regions. (a) Schematic of the Dutch coast with different types of river plume fronts: tidal plume front (TPF), inner front (IF) of entire plume, outer front (OF) of entire plume, and relic tidal plume fronts (RF). (b) Copernicus Sentinel-1 C-band synthetic-aperture radar image at day 10-02-2015 06:00 (HW + 0.5 h). This data has a spatial resolution down to 5 m. There are no Sentinel-1 images during the field campaign. Black dots are measurement locations M18 and M12. MV refers to Maasvlakte, which is the Port Extension. The ellipse indicates the anti-cyclonic rotation of the surface tidal velocity, where flood is in northeast direction, and ebb is southwest direction. The horizontal and vertical axes are displayed in RD coordinates in km. The coordinate system is defined that x is the cross-shore direction, and *y* the alongshore direction. The gray dotted lines and arrows highlights the location of panel b within panel a.

1.1. Background

A river plume can be divided into different dynamical regions: the near-field, the mid-field and the far-field plume (Garvine, 1984; Horner-Devine et al., 2015). A detailed description of the dynamics of the near-, mid- and far-field for a prototypical river plume can be found in Horner-Devine et al. (2015) (see their figure 2). The near-field is the area closest to the river mouth, where the momentum of the discharged river water dominates over the buoyancy of the plume layer. The near-field evolves into the mid-field, where Earth's rotation becomes important turning the plume toward the coast. Ultimately, a density driven coastal current is formed, which is known as the far-field plume.

The entire plume is bounded by a front, also referred to as the outer front (OF), separating from the denser seawater. This frontal boundary is mainly observed in large scale plumes, such as the Columbia River, Delaware Bay, Chesapeake Bay and Hudson River plume (Garvine, 1995; Horner-Devine et al., 2015). This offshore front is in thermal wind balance and moves on- and offshore due to the wind (Fong & Geyer, 2001; Fong et al., 1997). In addition, an inner front (IF) has been observed that separates the shallow coastal waters from the river plume, and that extends along the entire length of the river plume, from the river mouth to the far-field (Figure 1a). This IF has been observed to move offshore under upwelling favorable winds by Fong and Geyer (2001) and by tidal straining by de Boer et al. (2007).

In systems where the estuarine outflow is modulated by the tide, a near-field plume is formed on every ebb and is referred to as a tidal plume (Garvine & Monk, 1974; Horner-Devine et al., 2009; Kilcher & Nash, 2010; Luketina & Imberger, 1987; Marmorino & Trump, 2000). Tidal plume fronts (TPFs) are formed at the leading edge of the tidal plume and are associated with strong horizontal convergence, which can lead to strong downwelling on the order of cm/s (O'Donnell, 1988). The persistence of the TPFs is related to the freshwater discharge released from the river mouth on every ebb tide. At the river mouth the freshwater lifts off to form the TPF. The Columbia River TPF, with an annual mean discharge of 10,000 m^3/s, lasts for approximately 6–9 h after low water, but is sometimes still visible after 12–14 h when a new TPF is formed (Horner-Devine et al., 2009; Kilcher & Nash, 2010). Vertical and horizontal density differences due to previous tidal plumes,

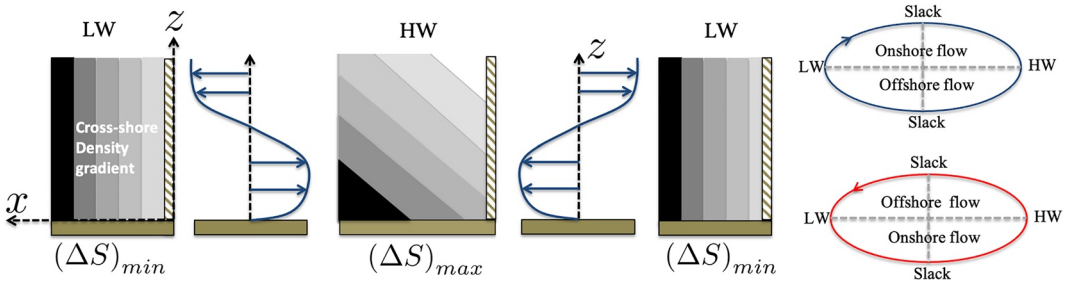

Figure 2. Schematic of cross-shore tidal straining along the Dutch coast, where the cross-shore current resulting from the modification of tidal ellipses interacts with the horizontal density gradient. The gray colors refer to water density, where darker is denser. ΔS refers to top-bottom salinity difference. LW refers to low water and HW refers to high water. The two ellipses are a near-surface (blue) and a near-bottom (red) tidal ellipse, which rotate anti-cyclonically and cyclonically respectively (clockwise and anti-clockwise in the Northern Hemisphere). The figure is based on Flores (2018) (Figure 1.3).

lead to complex fronts and the generation of internal waves (Kilcher & Nash, 2010; Nash & Moum, 2005). In contrast, the river Teign at Teignmouth UK, with a small discharge of 5 m^3/s, forms a TPF that dissipates after roughly 4.5 h (Pritchard & Huntley, 2006). TPFs of a surface advected river plume are often associated with elevated turbulence (Horner-Devine et al., 2013; Luketina & Imberger, 1987; O'Donnell et al., 2008; Orton & Jay, 2005) and have been observed to impact the seabed at depths up to 60 m (Orton & Jay, 2005). Despite their importance, little attention has been paid to TPFs and their evolution in shallow frictional systems, such as the Rhine ROFI.

In the near-field, the dynamics of these TPFs are similar to non-rotating buoyant gravity currents observed in laboratory and theoretical studies (Benjamin, 1968; Britter & Simpson, 1978; Kilcher & Nash, 2010; Luketina & Imberger, 1987; Marmorino & Trump, 2000; Yuan & Horner-Devine, 2017). In reality, however, TPFs seldom spread symmetrically, as observed in the Columbia River plume (Jay et al., 2009), or in the Connecticut River plume, where the lateral propagation of a part of the TPF is hindered by a tidal cross-flow (Garvine, 1974; O'Donnell, 1988, 1990). O'Donnell (1988) showed that this asymmetrical spreading led to an increased thickness of the hindered front.

1.2. Description of the Frontal Structure in the Rhine ROFI

The Rhine ROFI is formed by the discharge of the Rhine-Meuse rivers, with an annual mean discharge of 2,300 m^3/s, into the shallow Southern North Sea. As a result of strong tides, stratification and frictional effects, elliptical tidal currents are generated and dominate the dynamics of the Rhine ROFI through tidal straining and alongshore advection (de Boer et al., 2008; Simpson & Souza, 1995). Cross-shore tidal straining is the interaction of the horizontal density gradients with cross-shore shear, producing a semi-diurnal cycle of stratification (Simpson et al., 1990) (Figure 2). This requires the occurrence of a strong vertical cross-shore velocity shear. Observations and modeling of the Rhine ROFI describe several different fronts that are differentiated based on their generation mechanism. These observations indicate that 10 km downstream TPFs are still important, suggesting that the observations are located within the mid-field plume (Flores et al., 2017; Rijnsburger et al., 2018a). Throughout this study downstream is northeast from the river mouth, following the propagation direction of a Kelvin wave. Figure 1a indicates the different regions within the Rhine ROFI based on several observational and numerical studies (de Boer et al., 2008; Flores et al., 2017; Horner-Devine et al., 2015; Rijnsburger et al., 2018a). Additionally, Figure 1a summarizes a conceptual picture of the different fronts in the Rhine ROFI, which will be further clarified using the modeling described in this work. In particular, we differentiate fronts of two types: TPFs and IFs.

1.2.1. Tidal Plume Fronts

Modulation of the river outflow by the semi-diurnal tide results in the formation of a new TPF on every ebb (de Ruijter et al., 1997; Hessner et al., 2001; van Alphen et al., 1988) (Figure 1a). The progressive tidal wave along the Dutch coast inhibits the TPF from spreading radially during the ebb, leading to an arrested

front toward the northeast of the river mouth (Hessner et al., 2001). At that moment the previously released (relic) tidal plume is carried to the southwest, toward the arrested new front (van Alphen et al., 1988). Then the newly formed TPF propagates away from the mouth to the northeast due to its intrinsic speed and tidal advection at the start of the flood tide, moving quickly over a distance of 10–13 km in 4–6 h (Hessner et al., 2001; van Alphen et al., 1988). Using radar images and idealized numerical modeling, Hessner et al. (2001) found that the shape and location of the TPF in the near-field is strongly influenced by the phase of the semi-diurnal tidal cycle, and is only weakly influenced by the discharge volume, residual currents and spring-neap tidal cycle.

Field observations 10 km downstream of the river mouth, showed the onshore propagation of fronts which were associated with the TPF, and had features in common with TPFs in other systems, such as a plunging head and similar propagation speed (Flores et al., 2017; Horner-Devine et al., 2017; Rijnsburger et al., 2018a). These field observations demonstrated the importance of the semi-diurnal tide on the dynamics of the TPF, consistent with the results of Hessner et al. (2001). The tide controls the propagation of the fronts mainly by advection (Rijnsburger et al., 2018a), as a result of much larger ambient coastal currents than intrinsic frontal speeds. This is supported by scaling the typical maximum values for frontal speeds (uf) and ambient tidal currents (u0), leading to a ratio of $u_f/u_0 \approx 0.5/1 \approx 0.5$ (de Kok, 1997; Rijnsburger et al., 2018a). This ratio suggests the importance of advection in this system. In addition, downwelling winds were found to increase the downstream advection of the TPFs, while upwelling winds were found to decrease the advection (Rijnsburger et al., 2018a).

1.2.2. Inner Fronts

A second type of front is observed in the Rhine ROFI, which forms a boundary between the river plume and the inner shore along the coastline over a distance of about 100 km. This is referred to here as the IF (Figure 1a). As described in the idealized numerical model study of de Boer et al. (2007), the formation process of the IF is a consequence of the fact that the Rhine ROFI is advected off- and onshore every tidal cycle due to tidal straining. Visser et al. (1994) found that the tidal currents rotate as counter rotating ellipses between the surface and the bed (see schematic of an ellipse in Figures 1a and 2), as a result of the interaction between the progressive tide, stratification, friction and Earth rotation. The surface currents are offshore directed from low water (LW) to high water (HW), and onshore directed from HW to LW (Figure 2). The bottom currents are directed in the opposite direction as the surface currents. Accordingly, the IF moves approximately 5–10 km offshore between HW−3 and HW+3 leading to upwelling of colder water at the coast de Boer et al. (2007).

1.2.3. Spatial Frontal Structure

The Copernicus Sentinel-1 C-band synthetic-aperture radar image shows a multi frontal structure in the Rhine ROFI (Figure 1b). Several recent studies (Flores et al., 2017; Horner-Devine et al., 2017; Rijnsburger et al., 2018a) confirm the presence of multiple fronts within the Rhine ROFI. These fronts were observed in field-data collected at two mooring sites roughly 10 km downstream from the river mouth (Figure 1b). However, these data did not allow them to investigate the spatial movement of these fronts or how they interact. Additionally, difficulties arose to identify and differentiate between the inner and TPFs in the field data because their predicted arrival time is similar (Horner-Devine et al., 2017). Furthermore, these studies suspected the presence of more fronts in addition to the IF and the most recently released TPF (Figure 1). One of the motivations to investigate the dynamics of these fronts is that TPFs were shown to be able to increase bed stresses leading to resuspension (Flores et al., 2017; Rijnsburger et al., 2018a). Additionally, radar images showed that these fronts propagate toward the coast generating a cross-shore exchange flow that causes offshore sediment transport (Flores et al., 2017; Horner-Devine et al., 2017).

We use a three-dimensional realistic numerical model that complements existing field studies in order to better understand the spatial structure and movement of fronts in the Rhine ROFI. Specifically, we investigate the evolution of the TPF, the occurrence of multiple TPFs, and the processes responsible for the evolution of the front. The study area is restricted from the river mouth up to 20 km downstream, and from the coast to 30 km offshore. Here, we will use a hydrostatic model to investigate the TPFs, although fronts are non-hydrostatic. The hydrostatic model will only resolve the large scale properties as mentioned in Ralston et al. (2017).

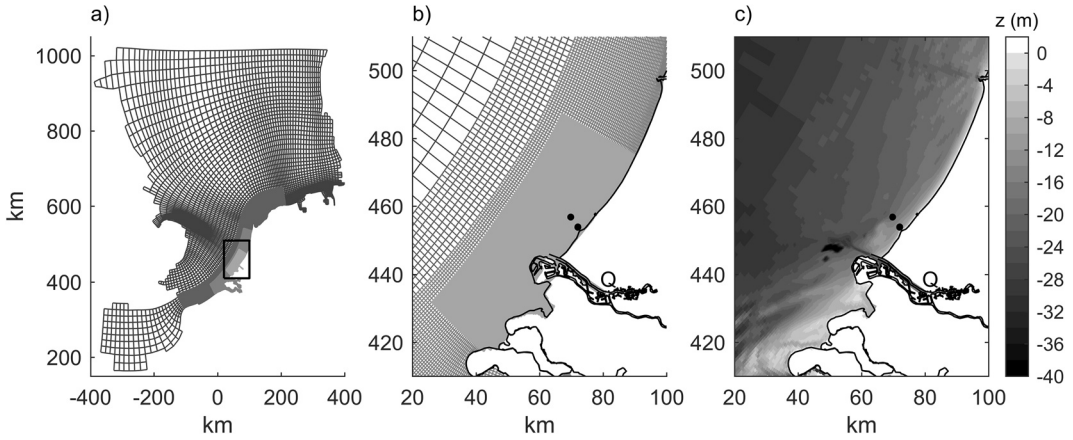

Figure 3. Model grid and bathymetry. (a) The entire model domain consists of four grids with different resolution. (b) Zoom on model grid along the Dutch coast. (c) Model bathymetry along the Dutch coast. Black dots are measurement locations, and Q refers to the discharge location at the river in the model. The horizontal and vertical axes are displayed in RD coordinates (in km).

The paper is organized as follows: In Section 2, we describe the model set-up and the field-data used. In Section 3, the model results are compared to in-situ data to evaluate the model performance. In Section 4 we differentiate between the different fronts, investigate the dynamics of the TPFs, and the processes responsible for the multiple front system. We discuss the findings and ask ourselves how generic these fronts are in Section 5. Finally, conclusions are presented in Section 6.

2. Methods

2.1. Numerical Model Configuration

The FLOW module of Delft3D is used to simulate a hindcast of flow and transport in the Rhine ROFI for the period of September 15 to October 07, 2014 (yeardays 258–280). Delft3D-Flow solves the three dimensional non-linear shallow water equations using the Boussinesq and hydrostatic pressure approximation (Deltares, 2014; Stelling & Van Kester, 1994), and has been used for different applications in shallow seas, coastal areas and estuaries (de Boer et al., 2006; de Nijs & Pietrzak, 2012; Lesser et al., 2004). For this study we use a model setup describing the southern North Sea with increased horizontal resolution toward the Dutch coast using a domain decomposition technique (Deltares, 2014). This decomposition results in four curvi-linear computational grids with increasing grid size: a coarse, intermediate, fine and extra fine grid (Figures 3a and 3b). The refinement is in both horizontal directions by a factor 3, 2 and 3 between coarse-intermediate, intermediate-fine and fine-extra fine, where the finest grid has grid cells between 80–400 m in alongshore direction and 80–500 m in cross-shore direction. All four grids contain 20 non-equidistant sigma-layers in the vertical, with smaller cells at the surface and bottom. These vertical cells have a size in the range of 3%–6% of the entire water column. This implies that the vertical resolution varies depending on the local water depth.

The model was forced on the northern and western boundaries by the astronomical tide, where the tidal constituents were obtained from the Dutch Continental Shelf Model (DCSM) (e.g., Verboom et al. (1992); Verlaan et al., 2005). A space- and time-varying wind speed (at 10m height) and atmospheric pressure has been applied at the free-surface obtained from the numerical weather prediction High-Resolution Limited Area Model (HiRLAM). In addition, a heat-flux model accounts for the exchange of heat through the air-sea interface using wind speed, air temperature (at 2 m), cloud coverage and relative humidity from the same meteorological model (HiRLAM). The incoming solar radiation is computed based on the latitude and time. Additionally, 85 rivers discharging into the southern North Sea are implemented, under which the Meuse and Rhine Rivers are the most important. Time-varying values of the Dutch rivers are used based on the available data (Rijkswaterstaat). The temperature and salinity for the rivers in the coarser grids are set to 11° and 0 PSU, while for the Dutch rivers the temperature and salinity are based on observations. Figure 4

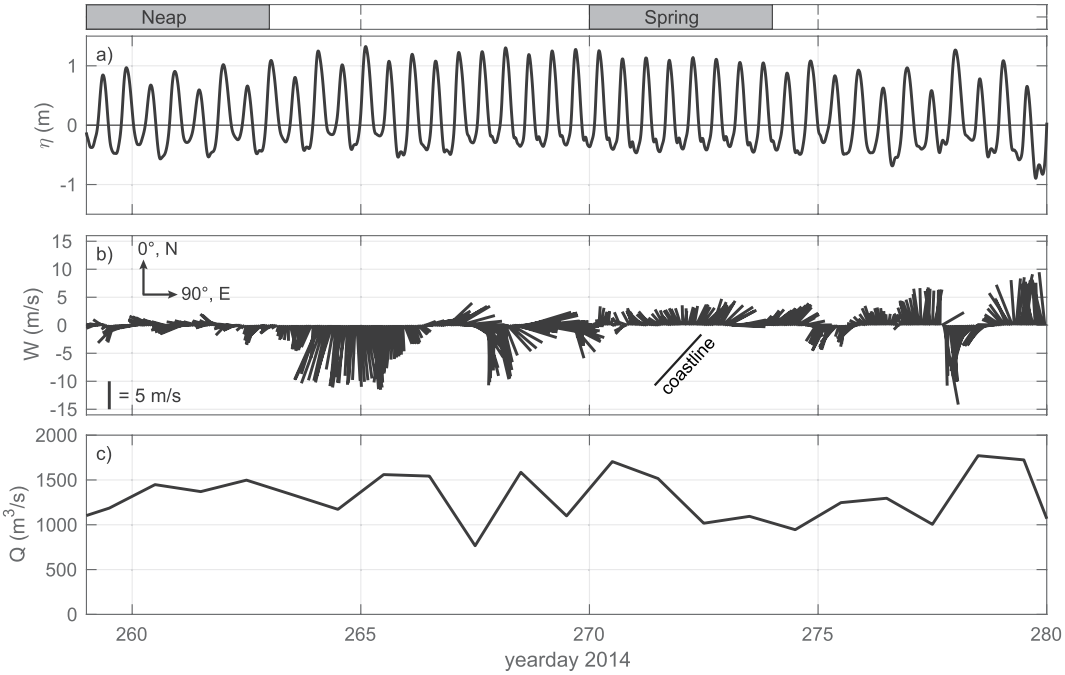

Figure 4. Time series of model forcing during two months in 2014 (September 15 till October 07, 2014). (a) Sea surface height (m) at station M18. (b) Wind vectors in m/s at station M18. (c) Discharge of Rhine River in numerical model (m^3/s).

shows the sea surface elevation, wind vectors at station M18 and the discharge at the river mouth corresponding to the period when field data was collected.

Space-varying bathymetry has been used in the model which is obtained from the North West European Shelf Operational Oceanographic System (NOOS) for the coarser grids, and based on surveys carried out by the Dutch Hydrographic Service and Rijkswaterstaat for the finer grids. The bathymetry of the Sand Engine and the Port extension have been implemented in the model based on bathymetry data from year 2014 (Figure 3c). The southern North Sea has a maximum depth of about 20–30 meters in the waters more offshore and in the navigation channel.

The model uses the k-ϵ model to resolve vertical mixing of salt, temperature and momentum. A background vertical diffusivity of $1 \cdot 10{-}5$ m^2/s and a horizontal diffusivity of 1 m^2/s are imposed on all grids. In addition, a background vertical viscosity of $5 \cdot 10^{-5}$ m^2/s is applied to all grids. A horizontal background viscosity of 5, 2.5, 1.25 and 1.25 m^2/s is applied to the coarse, intermediate, fine and extra fine grid. A larger horizontal viscosity of 250 or 1,000 m^2/s is applied to boundaries between different grids to prevent instabilities.

The model was initialized with a salinity of 34.5 PSU and a temperature of 11°, which is based on the long term average for the North Sea (Suijlen & Duin, 2002). North and east velocities were rotated into along- and cross-shore direction using a rotation angle of 42.5° from the North, where positive velocities are in northeast and offshore direction. The coordinate system throughout this study is defined as x is offshore directed and *y* is alongshore directed (Figure 1b). The spin-up period was 8 months, such that the impact of the initial conditions was limited. A numerical time step of 48 s has been used. The model has been set-up for the entire year 2014. However, this study is focused on a typical neap and spring period, this is because the Rhine ROFI responds differently during these periods as a result of the amount of tidal mixing (de Boer et al., 2006; Simpson et al., 1993). We selected a neap tide with relatively low wind speeds from the east (90°, <=5 m/s, days of the year 259–263), and a spring tide with relatively low wind speeds mainly from the southeast to southwest (135–225°, <6 m/s, days of the year 270–274), which coincide with the STRAINS field-campaign in 2014 (Flores et al., 2017) (Figure 4). These periods are referred to as a relatively calm neap and spring.

2.2. Field-Data

Field-data is used to investigate the model performance. Moorings and frames were deployed from September 17 until October 17, 2014 (yeardays 260–290) 10 km northeast of the mouth of the Rotterdam Waterway at 2 and 6 km offshore, corresponding to water depths of 12 and 18 m (Figures 3b and 3c black dots). In total, nine Sea-Bird MicroCAT conductivity temperature depth (CTD) instruments were attached to the two moorings, 4 at the 18 m site and 5 at the 12 m site. The CTD instruments were located at 12 and 18 m sites at 1, 3, 7, 8, and 10.5 m below the sea surface and at 1, 2.5, 10, and 15 m respectively, thus providing a detailed description of salinity and density throughout the water column at both sites. Vertical velocity profiles were measured using a four beam acoustic Doppler current profiler (ADCP) attached to a bottom frame sampling at a frequency of 1 Hz. North and east velocities were rotated into along- and cross-shore direction using a rotation angle of 42.5° from the North, where positive velocities are in northeast and offshore direction. Here, we used a 10 min average of the CTD and ADCP data. For more details see Flores et al. (2017) and Rijnsburger et al. (2018a).

2.3. Passive Tracers

Passive tracers, similar to dye injection, are added to the model simulations to follow the freshwater outflow from the Rhine-Meuse Delta (Figure 3). Passive tracers are released 2 h before until 2 h after low tide on four consecutive tidal cycles at the same location as the discharge (Figure 3c, Q). The timing of low water is determined by the M2 tidal constituent. It takes about 0.5 day for the tracer to leave the Rhine River mouth. Each tracer starts with a concentration of 1 kg/m^3, while a background concentration of 0 kg/m^3 is used. We define the contour of a tidal plume as the concentration where at least 85% of the tracer concentration was within this contour. This choice is made based on the salinity gradient, where we found agreement between 85% of the tracer concentration with salinity gradients larger than 2 PSU/km (Figures 12 and 13 in Section 4.4).

2.4. Front Identification and Properties

The fronts are identified using the horizontal salinity gradient, which is defined as

$$\left|\nabla_h s\right| = \sqrt{(\partial s \,/\, \partial x)^2 + (\partial s \,/\, \partial y)^2}\,, \tag{1}$$

where $(\partial s/\partial x)_n = (s_{n+1} - s_{n-1})/(x_{n+1} - x_{n-1})$, and similar for $\partial s/\partial y$ in the y-direction. The subscript n refers to a gridcell, and a central difference scheme has been used to calculate the gradients. In addition, more quantities are used throughout this study that highlight the location of the fronts, such as passive tracers (kg/m^3) and horizontal divergence, $Div_h = \partial u/\partial x + \partial v/\partial y$. The passive tracers isolate the different TPFs, because each tracer refers to a different release of freshwater from the river mouth. The fronts are expected to relate to a convergent flow ($Div_h < 0$), which should lead to downwelling at the leading edge of the frontal head (O'Donnell et al., 1998).

Salinity and salinity gradients are used to identify the fronts, as density is dominated by salinity in the Rhine ROFI. A sensitivity study of the choice of the magnitude of the salinity gradients was carried out and the 4 PSU/km was found to identify the newly released TPF, while gradients of 0.8 PSU/km were used to study the inner and outer fronts. A comparison with the tracers supported the robustness of this approach.

The TPF is followed in time and space to analyze the evolution of its properties, such as frontal speed and frontal Froude number. The TPF is identified by $|\nabla_h s|$ close to the river mouth at the beginning of the flood. We select a point on this front that we then follow. Subsequent locations on the front are calculated using a Lagrangian tracking method:

$$x_{t1} = x_{t0} + (\Delta t \cdot u_{t0}) \tag{2}$$

$$y_{t1} = y_{t0} + (\Delta t \cdot v_{t0}), \tag{3}$$

where x_{t0}, y_{t0}, u_{t0}, and v_{t0} are the frontal position and the surface velocities at the current time step on the salinity gradient, which can be in the middle, more toward the ambient side or toward the plume side of the gradient. Δt is the time step, which is 8 min. x_{t1}, y_{t1} refer to the new position of the front on the next time step. Then, we use $|\nabla_h s|$ to verify that we are still on the front. However, no corrections are made when the position deviates slightly from the gradient. When the trajectory gets off the gradient, for example, after one tidal cycle, we discard that data. This procedure results in a front trajectory in time and space on which we calculate the different properties. We use three different locations on the front trajectory to calculate front properties, which are (a) on the front, (b) ahead of the front, and (c) behind the front. The coordinates two steps back in time are used as the location behind the front, and the coordinates two steps forward in time are used as the location ahead the front. This means that the distance between these positions changes in time. The trajectory is not smoothened in time or space. A TPF cannot be represented well by one point, so we select 9–12 locations on each TPF, resulting in 9–12 front trajectories.

There are multiple definitions of Froude numbers (see for example Kilcher & Nash, 2010). Here, we use the frontal Froude number in line with other front studies (Britter & Simpson, 1978; Garvine & Monk, 1974; Horner-Devine et al., 2013; Kilcher & Nash, 2010; Luketina & Imberger, 1987), which is defined as the ratio of the frontal speed relative to the long wave phase speed behind the front:

$$F = \frac{u_f}{c_0}, \tag{4}$$

where u_f is the intrinsic frontal speed, c_0 is the linear long wave phase speed behind the front (excluding velocity shear). The linear long wave phase speed c_0 is calculated with the Taylor Goldstein equation only using density profiles. We calculate c_0 without shear to be in line with the other front studies (Garvine & Monk, 1974; Horner-Devine et al., 2013; Kilcher & Nash, 2010; Luketina & Imberger, 1987). However, the presence of a strong velocity shear will change c_0, and therefore F. The frontal Froude number compares the frontal momentum with the buoyancy of the tidal plume. The front is supercritical ($F > 1$) when the momentum dominates over buoyancy, meaning that information (for example internal waves) can only travel downstream.

The frontal speed moving with the front, u_f, is estimated on the front trajectory as $u_f = (\partial x / \partial t) - \overline{u_0}$, where $\overline{u_0}$ is the front normal depth mean ambient current ahead of the front. Therefore, u_f is relative to the background current (intrinsic frontal speed).

In this study, we define the strength of the fronts based on the horizontal salinity gradient. We chose the horizontal salinity gradient as a strength parameter, because of the definition of a front in the field. If there is no salinity gradient observed, there is no front. A sharp and large horizontal salinity gradient is defined as a strong front, while a diffuse low salinity gradient is defined as a weaker front (Jay et al., 2009).

2.5. Frontogenesis Equation

We use the frontogenesis equation to understand the processes controlling the evolution of the TPFs. The frontogenesis equation describes the evolution of a scalar gradient by deriving the scalar tendency equation in the front normal direction (O'Donnell, 1993; Geyer & Ralston, 2015; Giddings et al., 2012; Akan et al., 2018). Here, we chose the salinity (s) as scalar, because the density in this system is dominated by salinity. We apply the frontogenesis equation in a Lagrangian framework, so in other words we are moving with the front. At each front location (x, y, t), a local grid front in front normal and parallel direction is made. Then, all properties are interpolated to this grid. This grid is used to calculate gradients in front-normal and front-parallel direction. The frontogenesis equation in front-normal direction (n) reads as follows:

$$\underbrace{\frac{D}{Dt}\left(\frac{\partial s}{\partial n}\right)}_{\text{total derivative}} = \underbrace{-\frac{\partial u_n}{\partial n}\frac{\partial s}{\partial n} - \frac{\partial u_p}{\partial n}\frac{\partial s}{\partial p} - \frac{\partial w}{\partial n}\frac{\partial s}{\partial z}}_{\text{horizontal differential advection}} \underbrace{- \frac{\partial}{\partial n}\frac{\partial}{\partial z}\overline{s'w'}}_{\text{vertical mixing}} \tag{5}$$

Table 1
Root-Mean-Squared Error and Bias for the Stations M18 and M12 for Surface and Near Seabed (Bed) Salinity (PSU), Alongshore (v) and Cross-Shore (u) Velocity (m/s)

	RMSE sal		RMSE v		RMSE u		Bias sal		Bias v		Bias u	
Station	Surface	Bed	Surface	Bed	Surface	Bed	Surface	bed	Surface	Bed	Surface	Bed
M18	1.93	1.25	0.16	0.08	0.15	0.07	0.52	−1.12	0.008	0.014	−0.0055	0.0043
M12	1.93	1.99	0.15	0.10	0.12	0.08	−0.5	−1.75	−0.018	0.02	−0.028	0.0006

where n, p, and z denote the front-normal, front-parallel and vertical coordinates, u_n, u_p, and w are the velocities in these directions. The total derivative on the left side of the equation is balanced by four terms. The first term on the right hand side represents the enhancement (reduction) of the alongshore salinity gradient in the presence of convergence (divergence) (O'Donnell, 1993). The second term represents horizontal differential advection of the salinity gradient in the presence of a front-parallel salinity gradient, which could be interpreted as shear on the fronts. The third term represents vertical differential advection of the salinity gradient in the presence of a vertical salinity gradient. The fourth term represents the front-normal gradient of vertical mixing (Geyer & Ralston, 2015). Positive or negative values of these terms either strengthen or weaken the gradient depending on the local conditions. These terms together generate, strengthen or weaken a front.

2.6. Cross-Shore Tidal Straining

Cross-shore tidal straining plays an important role for the large-scale circulation in the Rhine ROFI (de Boer et al., 2008; Simpson & Souza, 1995). Therefore, we want to assess the role of tidal straining on the dynamics of the fronts. The Potential Energy Anomaly Equation is often used in the Rhine ROFI to approximate tidal straining and other dominant processes (de Boer et al., 2008; Rijnsburger et al., 2016; Simpson & Bowers, 1981; Simpson et al., 1990). We calculate cross-shore tidal straining (Sx) by using the three-dimensional Potential Energy Anomaly Equation from de Boer et al. (2008) (for the entire equation and information see their Equation 8):

$$S_x = \frac{g}{H}\int_{-h}^{\eta} \tilde{u}\frac{\partial \overline{\rho}}{\partial x} z dz, \tag{6}$$

where u is the cross-shore component of the velocity, $\tilde{u} = u - \overline{u}$ is the deviation from the depth mean cross-shore velocity, ρ is the density (kg/m^3), g is the gravitational acceleration and H is the water depth. S_x is calculated over the finest grid and then interpolated to front trajectories.

3. Comparison of the Model With the Field-Data

This section validates the numerical model by comparison with the measurements of the field data for both a neap and spring period. The following key metrics are used when comparing to the STRAINS II field data: temporal salinity structure, vertical density structure, timing of the TPF, structure and magnitude of the tidal currents. Both the model and field-data are presented in the time zone UTC+1. Additionally, we calculate quantitative evaluation measures, such as the root mean square error (RMSE) and the bias, to assess the model performance for both mooring stations (See Table 1). This analysis is then followed by a comparison with previous modeling and field campaigns in the Rhine ROFI. This is done in order to highlight where the model agrees with these studies, as well as any key differences.

The agreement shown by the metrics in Table 1 is typical of ROFIs. The bias and RSME errors result from initialization fields, wind fields and because the sources and variability of freshwater are not well resolved within the input data (Brown et al., 2016). In the case of the velocity, this is due to the fact that we are not using all of the tidal components, together with the interactions with salinity. In general, the model is in good qualitative agreement with the field-data on the neap tide; with reasonable agreement on the spring

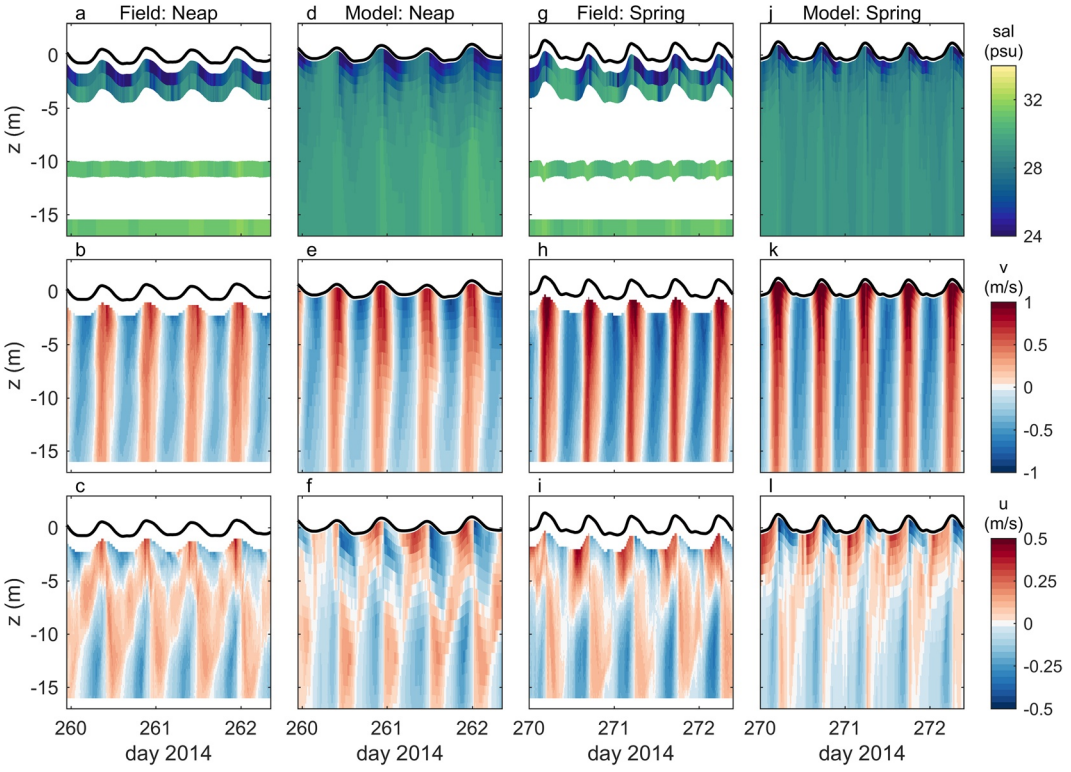

Figure 5. Comparison of field-data (a–c and g–i) and model (d–f and j–l) at station M18 for salinity, alongshore- (v) and cross-shore (u) velocity, where the x-axis is day of the year, y-axis is depth in meters. Two periods are plotted: neap (260–262.4) and spring (270–272.4). Positive velocities are in northeast and offshore direction, while negative velocities are in southwest and onshore direction.

tide, Figure 6. In the following, we will briefly highlight areas of agreement, as well as discrepancies between model and field data (Figures 5 and 6).

Despite the coarse vertical resolution of the field-data, vertical salinity and density profiles indicate a similar structure between model and field-data near the surface and the bed (Figures 5 and 6i–6l). This comparison shows good agreement for near surface salinity, while the near bed salinity is systematically fresher (Table 1). Additionally, the surface salinity and density demonstrates the passage of a TPF each tidal cycle after HW (Figures 5 and 8). Table 2 compares front arrival times between the observations and the model for the nine fronts shown in Figure 6, which shows a range between 10 and 40 min. This offset seems to align with the offset of the tidal elevation and current.

Overall, the model captures the vertical and temporal structure of the tidal velocity (Figures 5 and 6e–6h). A small delay in the modeled velocities is observed (Figures 6e–6h). The alongshore velocity is slightly overestimated in the model (Figures 6e and 6f). Additionally, the magnitude of the offshore velocity generally coincides with the field-data, while the onshore velocity is slightly overestimated (Figures 6g and 6h, Table 1). In general, the model captures the strong cross-shore shear that alternates during one tidal cycle. The modeled cross-shore velocity penetrates deeper into the water column during neap, while being thinner during spring. The same trend has been observed in the modeled vertical salinity resulting in an over- and underestimation of the pycnocline depth (Figures 5c, 5f, 5i and 5l). The timing and magnitude of the tidal velocities, in both directions, are in agreement with the observations and previous studies (de Boer et al., 2006; Simpson & Souza, 1995; Visser et al., 1994); we observe higher velocity magnitude during spring tides compared to neap tides and opposite cross-shore velocities in the top and bottom layers resulting in elevated velocity shear. This velocity structure with counter rotating top-bottom tidal ellipses is characteristic of the Rhine ROFI (Visser et al., 1994). The model also captures the interaction between the velocity shear and the horizontal salinity gradient resulting in the alternation of a stratified and well-mixed water column (Figure 5).

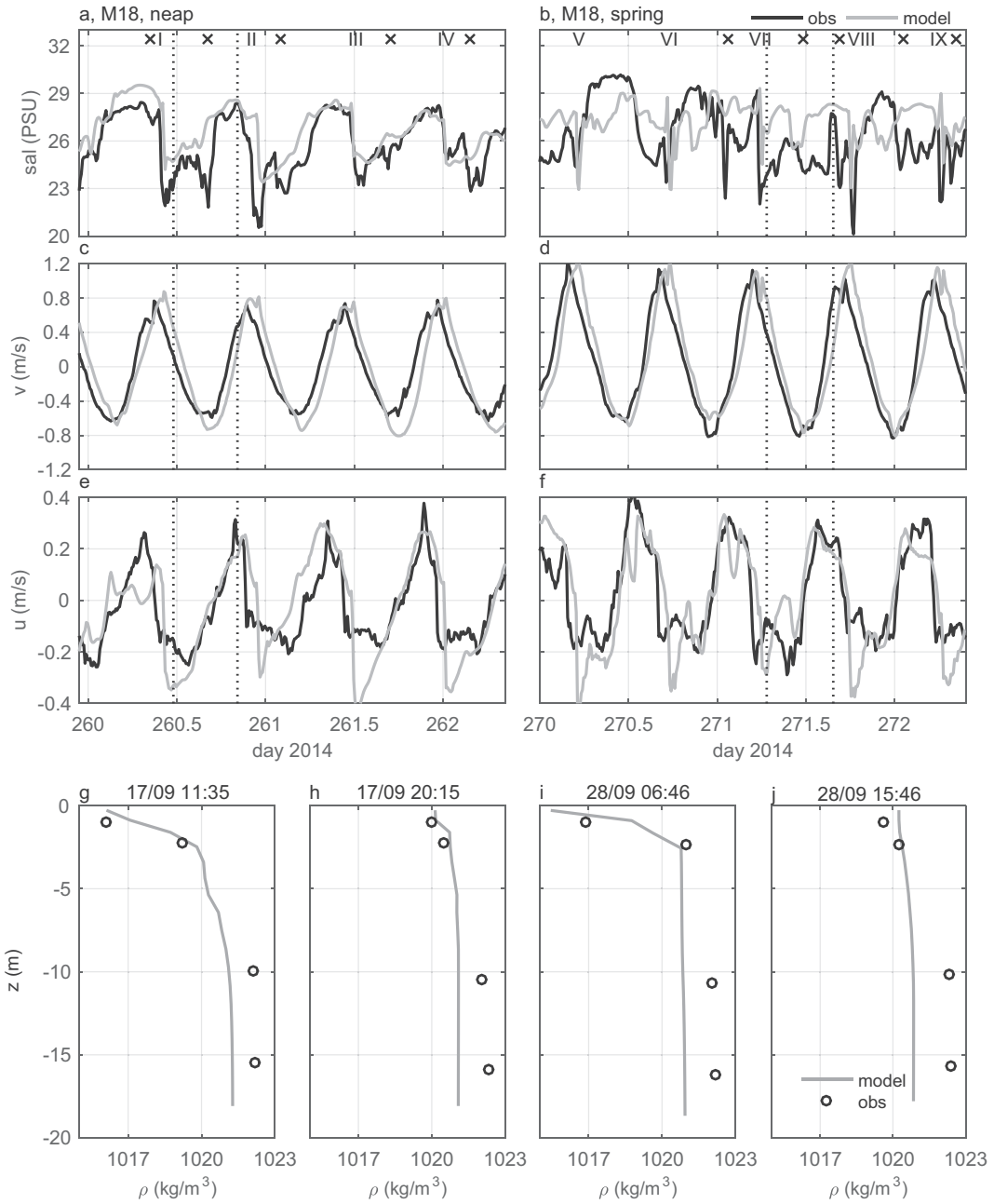

Figure 6. Comparison between model and field-data for a neap (left panels) and a spring tide (right panels) at station M18. (a–b) Surface density alongshore surface velocity (v), (e–f) cross-shore surface velocity (u), (g–j) vertical profiles of density. The sample times of vertical density profiles are chosen as follows: For each period (spring and neap) we choose a density profile occurring soon after a frontal passage, in order to show the stratification induced by it, and a density profile occurring hours after the front has passed but before the next one passes, in order to represent the well-mixed conditions that typically exist between frontal passages. The gray lines refer to the model data, and the black lines refer to the field-data. The black dotted lines in panels a–h refer to the vertical density profiles in panels g–j. In panels g–j, the black circles refer to the mooring data (observations). The roman numbers in panels a and b mark newly released TPFs, while the black crosses mark other fronts.

After validating the model prediction with field data, we turn to examining model predictions across the entire Rhine ROFI area. Therefore, we plot surface fields of salinity and the velocity vector during one tidal cycle to qualitatively compare the spatial structure with previous studies (Figure 7). As indicated by Figures 5 and 6, the surface currents rotate anti-cyclonically near the surface and cyclonically near the bed (not

Table 2
Arrival Times for the Fronts in Figure 6 for Both the Observations and Model Data

	Front I	Front II	Front III	Front IV	Front V	Front VI	Front VII	Front VIII	Front IX
M18	17/09	17/09	18/09	19/09	27/09	27/09	28/09	28/09	29/09
Obs	09:45	22:15	11:35	00:05	04:36	16:56	05:36	18:06	05:56
Model	10:15	22:55	11:45	00:15	04:56	17:26	05:56	17:56	06:26
Diff (min)	30	40	10	10	20	30	20	10	30

Note. The fronts are numbered from I to IX in accordance with Figure 6. The time difference between model and observations is given in minutes. Note that the data used for the validation is 10-minute averaged.

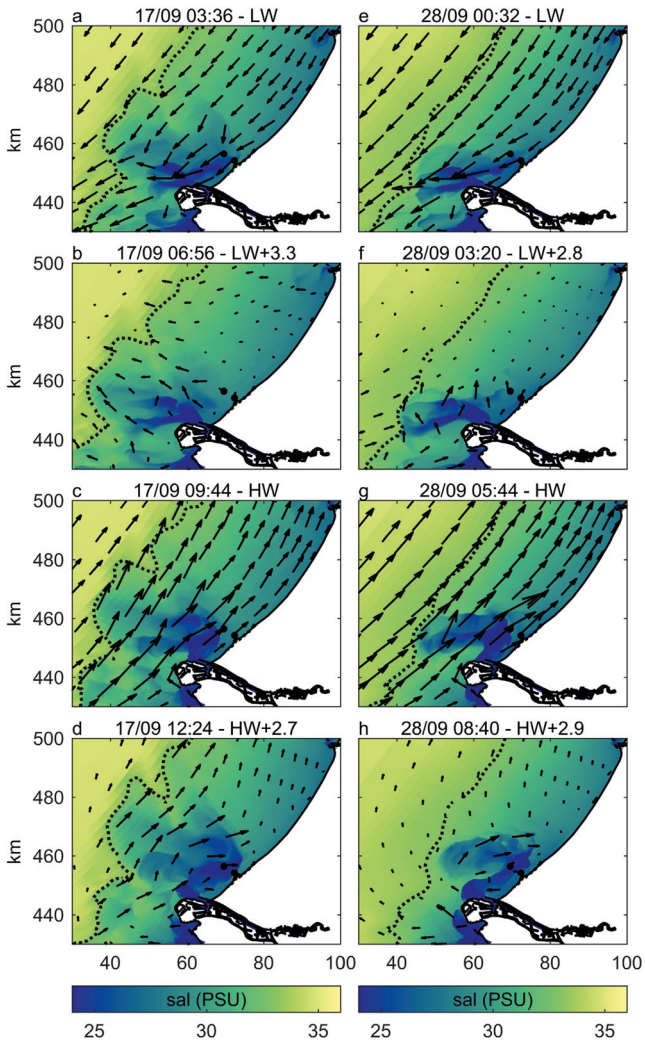

Figure 7. Surface salinity during one tidal cycle. The vectors represent the surface velocity. The first row represents low water (a and e), and the third row represents high water (c and g). The left column (a–d) is during the neap period on day 260 (17/09/2014) and the right column (e–h) is the spring period on day 271 (28/09/2014). The horizontal and vertical axes are displayed in RD coordinates in km. The dashed black line is the 33 PSU contour of salinity to mark the river plume. Black dots are measurement locations. The time zone is UTC+1.

shown) during one tidal cycle (Figure 7). The cross-shore surface velocities in the downstream plume are smaller during spring than during neap. These results are inline with the observations of Visser et al. (1994). In addition, the offshore salinity shows an OF that extends along the coast, with smaller horizontal salinity gradients found near the offshore boundary, in comparison to those found close to the river mouth. We highlight the offshore boundary by selecting a salinity contour of 33 PSU. The modeled anti-cyclonic surface circulation, and the cyclonic circulation near the bed during one tidal cycle, are in good agreement with previous model studies in the Rhine ROFI (de Boer et al., 2006, 2007, 2008; Fischer et al., 2009). Highlighting that the cycle of tidal straining is reproduced.

4. Results

4.1. Distinction Between Multiple Fronts

In this section we use the model to investigate the multi-frontal structure, focusing initially on a calm neap tide (Figure 4). We use the horizontal salinity gradient at the surface to identify the spatial frontal structure, the normalized horizontal divergence (Div_h/f) at the surface to identify regions of divergence (convergence) (O'Donnell et al., 1998) with $f = 1.15 \cdot 10^{-4}$ s^{-1}, and the concentration of a tracer to identify water associated with the newly released tidal plume (Figure 8). Three times within a tidal cycle are plotted coinciding with Figure 7: LW (03:36), HW (09:44), HW+2.7 h (around slack, 12:24). The horizontal salinity gradient shows many fronts in the near- and mid-field plume, with the largest gradients around the river mouth (Figures 8a–8c). The different fronts are labeled inline with Figure 1a. The inner and outer fronts are identified as the frontal features of the entire river plume with salinity gradients of 0.8 PSU/km and a salinity contour of 33 PSU, respectively. These fronts are indicated in Figures 8g–8i with gray and black dotted lines, and labeled as IF and OF. The TPF has a horizontal salinity gradient with a minimum of 4 PSU/km and is indicated in Figures 8g–8i as a dark red line and labeled as TPF. The other distinct fronts are indicated with label relic tidal plume fronts (RF). The interest of this study is mainly on the fronts around the river mouth and northeastwards. The following subsections will discuss the observations of the IF and the TPF.

4.1.1. Inner Front

The IF is visible in the salinity gradients in Figure 8a as a distinct straight line parallel to the coast. Its surface signature starts to appear around LW−2, and accelerates offshore after LW. The IF propagates offshore through the 18 m mooring site between LW and HW (Figures 8a and 8b).

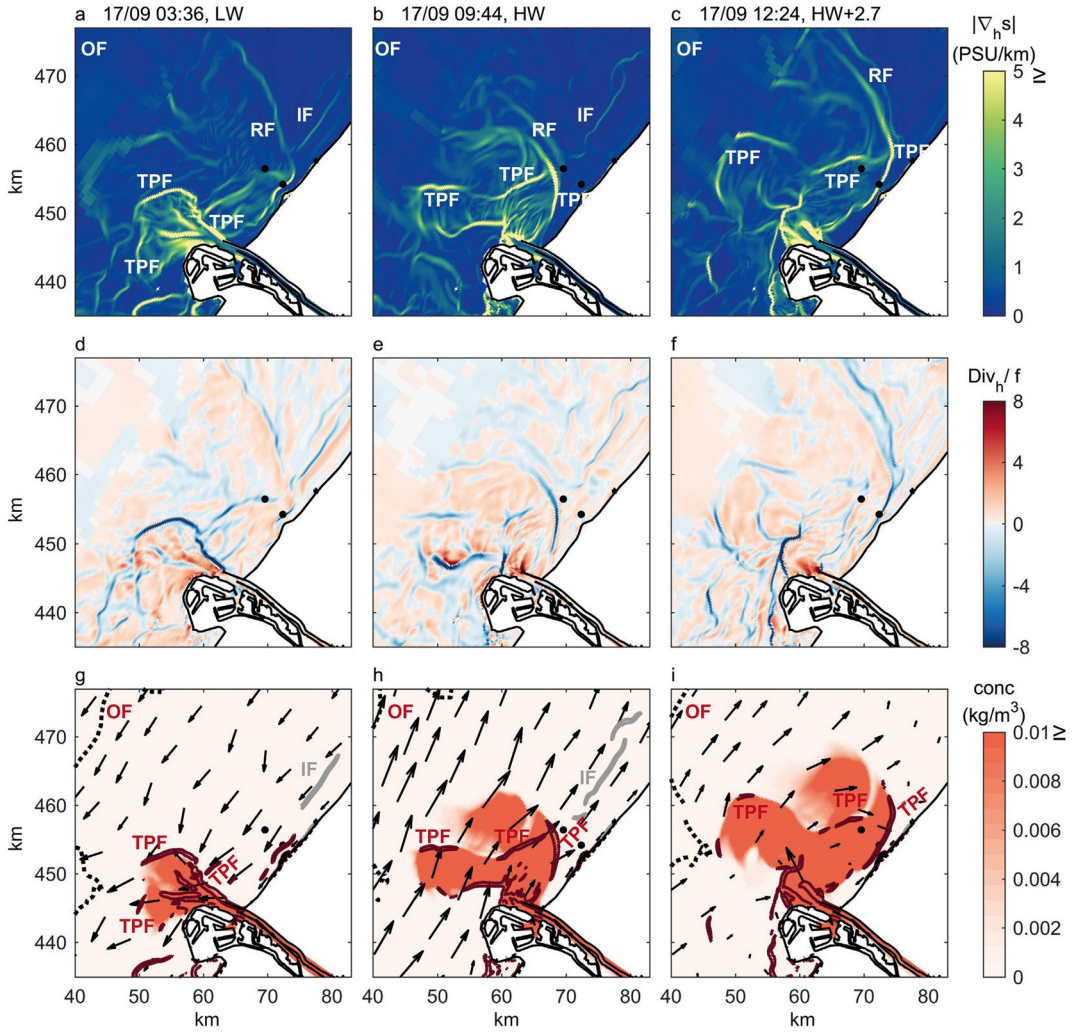

Figure 8. (a–c) Plan view of the absolute value of the horizontal salinity gradient, (d–f) normalized horizontal divergence (Div_h/f), and (g–i) a tracer concentration in the surface layer during a tidal cycle at a neap tide (day 260 or 17/09). Each column represents a snapshot in time, where low water (LW) is around 03:36, high water (HW) is around 09:44, and slack water around HW+2.7 h. The vectors represent surface velocity (m/s). The two black dots indicate the two mooring sites. The labels refer to the different fronts inline with Figure 1a. The black dotted line indicates the outer edge (OF) of the river plume using the 33 PSU salinity contour. The gray line highlights the inner edge of the river plume (IF), using the 0.8 PSU/km salinity gradient contour. The dark red solid line is the salinity gradient of 4 PSU/km or larger, highlighting the newly released tidal plume front (TPF). Older TPFs (relic fronts) are labeled with (RF). Note that a salinity gradient of 2.5 PSU/km parallel to the coast is observed around (62, 477) km. This gradient is an artifact due to the grid boundary. The horizontal and vertical axes are displayed in RD coordinates in km. See Supporting Information Movie S1 for the horizontal salinity gradient in time.

In addition, the IF stretches and moves downstream (northeastwards) between LW and HW (not shown). de Boer et al. (2007) found that this front propagated back onshore between HW and LW due to the onshore surface tidal currents. On this neap day the model shows that the IF dispersed between HW and HW+2.7. No clear onshore movement of the IF through the mooring site is observed based on the horizontal salinity gradient. The timing of offshore propagation is similar to the timing of tidal straining observed by Simpson and Souza (1995) and de Boer et al. (2007), which is the mechanism behind the generation of this offshore propagating front (de Boer et al., 2007). In the study of de Boer et al. (2007) the IF reached its most offshore location on HW, which is in line with what we have found here. The IF was located 6.4 km from the coastline at HW. Therefore, the cross-shore movement of the modeled IF stayed within the 5–10 km range observed by de Boer et al. (2007) in sea surface temperature images.

4.1.2. Tidal Plume Fronts

The high salinity gradients of 4 PSU/km or greater observed around the mouth at LW (03:36) correspond to the newly released TPF (Figure 8a). Here the newly released tracer concentration (Figure 8) is bounded by these high salinity gradients and can be used to identify this new TPF. However, the magnitude of these gradients differ around the tidal plume, such that the plume is not entirely bounded by gradients above 4 PSU/km threshold (Figures 8g–8i). The TPF is clearly indicated by negative divergence values ($Div_h < 0$, convergence), suggesting downwelling at the leading edge of the front inline with O'Donnell et al. (1998). The northern arc of the TPF (label TPF) is arrested by the ebb tide and initially remains attached to the mouth, while the southern arc of the TPF (label TPF) has a weaker salinity gradient due to the additional southward spreading by the ebb current (Figure 8a). These findings are in line with observations of Hessner et al. (2001), who found that during the ebb flow the northern arc of the TPF is arrested and strengthens.

The tidal plume increases in area during the tidal cycle (Figures 8g and 8h). The flood current then advects the tidal plume, and its TPFs, northeastwards. Consequently the arc of the northeastern TPF starts propagating to the north-east on the flood. The TPF then swings onshore until the next LW. At HW+2.7 (12:24) the northeastern TPF has passed through both of the mooring sites, and propagated at least 12 km northeastwards and toward the coast. This distance is in line with the findings of van Alphen et al. (1988) and Hessner et al. (2001) who found that the northeastern front moved about 10–13 km downstream during one tidal cycle.

In addition, Figures 8a and 8c shows fronts with horizontal salinity gradients between 1 and 4 PSU/km, which are not related to the most recently released TPF or IF. These fronts (RF) are wider with lower salinity gradients during the ebb compared to the flood. Additionally, these fronts seem to align with a convergent flow. In Section 4.4 we will investigate whether these other fronts are relic TPFs. First, we will explore the differences with a spring tide.

4.2. Comparison Between a Neap and a Spring Tide

The tide plays an important role in the stratification and structure of the Rhine River plume (de Boer et al., 2006; Simpson & Souza, 1995). During spring tide vertical stratification is expected in the near- and mid-field with little tidal straining in the far-field (de Boer et al., 2006; Simpson & Souza, 1995), while strong vertical stratification is present along the entire coast during neap tide. The lack of a horizontal salinity gradient in Figures 9a–9c indicates that an IF is not present during the spring period, which is in agreement with the results of de Boer et al. (2007). The tracer concentration in Figures 7i and 8i shows a similar area during the neap and spring period. The horizontal salinity gradient (label OF) shows that the outer edge of the river plume does not extend as far offshore during spring as found during neap. All the fronts around the river mouth are located within a radius of approximately 20 km (Figure 9).

The salinity gradients and the tracer concentration demonstrate the complexity of the system and the presence of strong TPFs (label TPF, >4 PSU/km) at some locations around the released tidal plume. The TPF to the southwest of the tidal plume is propagating southwestwards and offshore during ebb. The northeastern TPF is arrested on the northeastern side of the tidal plume due to the ebb flow (Figure 9a). Similar to neap, this northeastern TPF swings to the northeast and onshore during the flood period (Figure 9b). These gradients correspond to distinct regions of convergence (Figures 9d–9f).

4.3. Life Cycle of the Tidal Plume Front

The TPF controls the dynamics in the near-field, and affects the evolution of the entire river plume (Cole et al., 2020; Hetland, 2005). To understand the multi-frontal system, we first want to understand the life cycle and evolution of a TPF. Here, we follow the northeastern arc of four TPFs per neap and spring period (released on 16/09–17/09, 27/09–29/09). Throughout this study, we label these TPFs based on generation time for convenience; front 1 is generated first and front 4 last (colored as orange, red, blue and green respectively). The spatial structure and propagation of one neap and spring TPF is shown in Figure 10, where the period has been split into flood and ebb. The TPF is represented by 9–12 points, which are indicated by the small dots in Figure 10. As mentioned in Section 2.4, the front is followed using the direction and

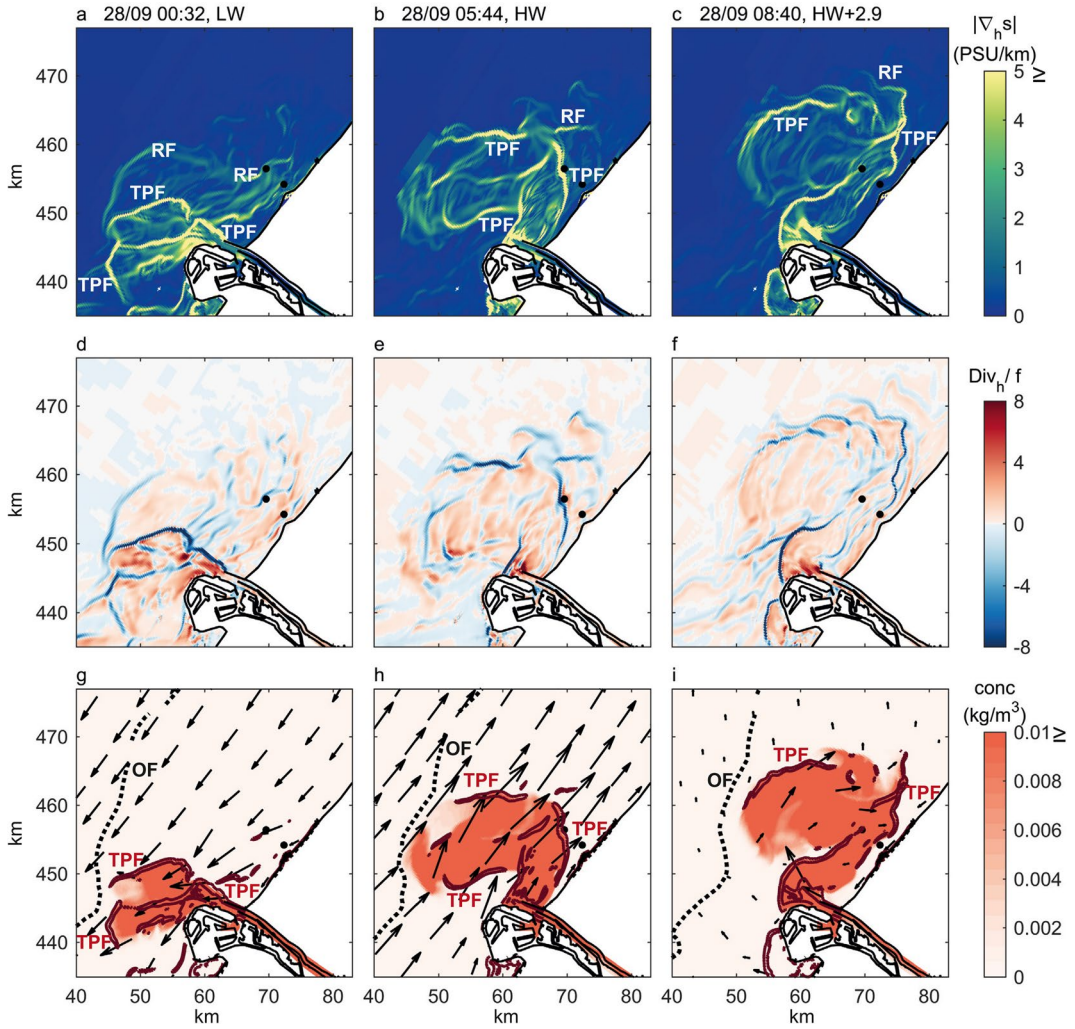

Figure 9. (a–c) Plan view of the absolute value of the horizontal salinity gradient, (d–f) normalized horizontal divergence (Div_h/f), and (g–i) a tracer concentration in the surface layer during a tidal cycle at a spring tide (day 271 or 28/09). Same description as Figure 8. See Supporting Information Movie S2 for the horizontal salinity gradient in time.

magnitude of the surface velocity, and only shown when the horizontal salinity gradient is at least 1 PSU/km and the trajectory is still on the front. The TPFs shown in Figure 10 refer to the same tidal cycle as in Figures 8 and 9, and are labeled as front 3.

During the first flood period the downstream edge of the TPF propagates in the northeast direction, turns onshore and gets close to the coast. The spacing between the lines showed that the front accelerated at the beginning of the flood and decelerated toward the end for both fronts. Additionally, Figures 10a and 10b show that the spring front moved faster than the neap front during the flood period, possibly because of higher tidal velocities or larger horizontal salinity gradients. When the tide reverses and the ebb current starts, both fronts are first stalled until the ebb flow accelerates and advects the fronts southwestward. The onshore part of the front is almost parallel to the coastline, while propagating southwestwards.

As discussed in Section 2.4, the total horizontal salinity gradient ($|\nabla_h s|$) is used to indicate frontal strength. An increase in $|\nabla_h s|$ is defined as a strengthening of the fronts, while a decrease is defined as a weakening of the fronts. This value is interpolated to the front trajectories and plotted in Figure 11 for the four TPFs together with the alongshore distance relative to the river mouth and the frontal Froude number and the tidal plume thickness behind the fronts. These properties are only plotted for two frontal trajectories per front, one trajectory that propagates downstream and one that propagates toward the coast (yellow dots

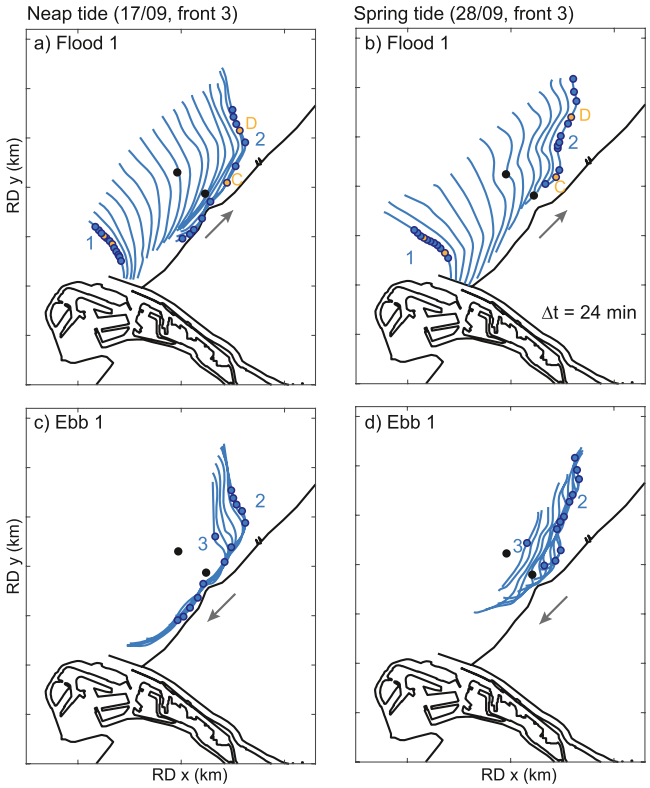

Figure 10. (a and c) Front traces for a neap tide and (b and d) spring tide. The trajectory has been split into flood 1 and ebb 1. Gray arrows and numbers show propagation direction. The time between lines is 24 min. This is the tidal plume front observed in Figures 8 and 9, which also refers to front 3 (the third release) in Figures 11–13. The line indicates that $|\nabla_h s| > 1$ (PSU/km), otherwise the trajectory ends. The dots at the beginning and sometimes at the end on the front traces show the location of the 9–12 trajectories per front followed in time. The yellow dots in panels a and b refer to the trajectories plotted in Figure 14, referred to as a downstream and coastal trajectory following the front (d and c, respectively). The horizontal and vertical axes are RD coordinates in km.

in Figure 10). The spring fronts have stronger horizontal gradients than the neap fronts, and travel a greater alongshore distance. The neap fronts traveled up to 20 km alongshore, while the spring fronts traveled up to 23 km alongshore (Figures 11i–11l). Almost all fronts reached a $|\nabla_h s| < 1$ (PSU/km) during the southwestwards propagation on the ebb, indicating a weakening of the fronts at 12–13 h after LW. Variability due to the neap and spring tides, as well as within each set of four consecutive neap and spring tracks is evident. This reflects the changing strength of the tidal currents, as well as changes in wind conditions, as also found by Rijnsburger et al. (2018a) in an analysis of the field data at the 12 m mooring site. The gradient shows differences along the northern arc and the properties at these two locations show differences.

The magnitude of the frontal Froude number (F) increases and decreases during flood (Figures 11m–11p). Maximum values of F are observed around HW for most trajectories (Figures 11m–11p). This is most apparent for the spring trajectories (Figures 11o and 11p). All TPFs are critical or supercritical at the beginning of the trajectory, which is consistent with established theories (Benjamin, 1968; Britter & Simpson, 1978; Shin et al., 2004). Note that this Froude number definition is based on gravity currents in laboratory studies without any shear flow. In river plumes, a three-dimensional flow field is present and strong velocity shears can be present influencing the dynamics of TPFs. We obtain subcritical frontal Froude numbers for all the fronts in Figure 11 if we include the vertical velocity shear in the calculation of c_0.

4.4. Evolution of a Tracer Concentration

The four TPF trajectories in Figure 11 ended 12–13 h after LW as the horizontal salinity gradient became lower than 1 PSU/km ($|\nabla_h s| < 1$). However, Figures 8 and 9 show the presence of weak fronts northeast of the newly released TPF. Therefore, we follow tracers to investigate whether these weak fronts are relic TPFs. The tracers correspond to the ebb release of the four consecutive TPF trajectories shown in Figure 11. Figures 12 and 13 show the total horizontal surface salinity gradient with contour lines for the four tracers in panels a and b. Panels c and d show the vertical structure of the alongshore horizontal salinity gradient with tracer contour lines. These contour lines contain a minimum of 85% of the tracer concentration at the surface (panels a and b) or along the cross-section (panels c and d). We define that the contours represent fronts, and the entire "circle" represents the tidal plumes. Here, we label the tidal plumes and fronts as in Section 4.3, where tidal plume (front) 1 is generated first and tidal plume (front) 4 the last (orange, red, blue and green respectively). Two different times are plotted per period, HW−0.4 and HW+0.8 h.

Both, the surface field and the cross-section demonstrate that the horizontal salinity gradients ahead of the TPF overlap with tracer contours, suggesting that these weaker fronts are relic TPFs (Figures 12 and 13; the orange and red lines). During neap, the tracer contours indicate that the relic front in panels a and c originates from the release on the previous tidal cycle (red line, second release; Figure 12). Between HW−0.4 and HW+0.8, the fronts are spreading and moving northeastward. The distance between the blue and red line decreases during the 1.2 h, suggesting that the blue front propagates faster than the red front (Figures 12a and 12b).

In general, the tracer contours demonstrate that a new tidal plume moves into a relic tidal plume. The tidal plumes spread and mix during each tidal cycle, resulting in the oldest tidal plume being wider, deeper and saltier with newer tidal plumes within it. The tracers show overlap between each other instead of separate pulses for both periods. During spring, the tracers stay horizontally quite confined but mix vertically. Therefore, after two tidal cycles, a tidal plume can already be mixed over the entire water column during

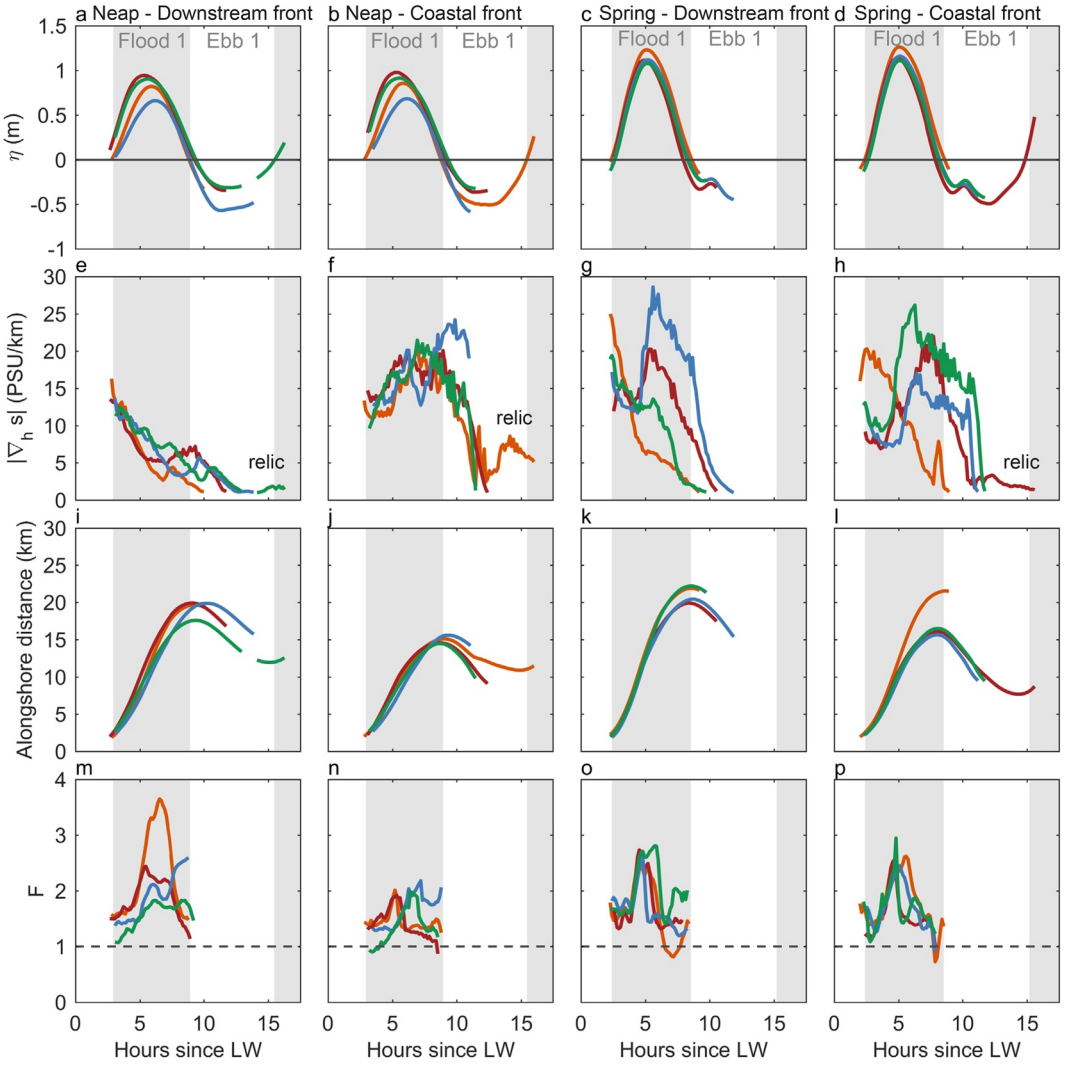

Figure 11. Front trajectories for (a, b, e, f, i, j, m, and n) neap (16/09–18/09, days 260–262) and (c, d, g, h, k, l, o, and p) spring (27/09–29/09, days 270–272) tide. Horizontal axis is hours since low water. Vertical axis is (a–d) the sea surface height (m); (e–h) the absolute horizontal salinity gradient (PSU/km); (i–l) the alongshore distance (km) from the river mouth, where northeastward is positive; (m–p) frontal Froude number. The four colors represent the four tidal plume fronts (TPFs) referring to a different tidal cycle: orange is front 1, red is front 2, blue is front 3 and green is front 4. The first and third column show a trajectory in downstream direction, while the second and fourth column display a trajectory toward the coast (see for example labels d and c respectively in Figure 10). The trajectory is ended when $|\nabla_h S| < 1$ (PSU/km) or roughly at the end of the flood period (for f and h). Three trajectories are selected where the TPF transitions into a relic front. The gray shaded areas refer to flood, and the white areas to ebb.

spring tide. This suggests that tidal mixing is larger during spring tide in line with previous studies (de Boer et al., 2006; Simpson et al., 1993). During neap the vertical mixing is less, resulting in a distinct fresher upper layer consisting of three different ebb releases (Figures 12c and 12d).

4.5. Frontogenesis

We use the frontogenesis equation (Equation 5) to investigate the processes that strengthen and weaken the fronts in the Rhine ROFI. Our analysis considers which terms in Equation 5 contribute to changes in the

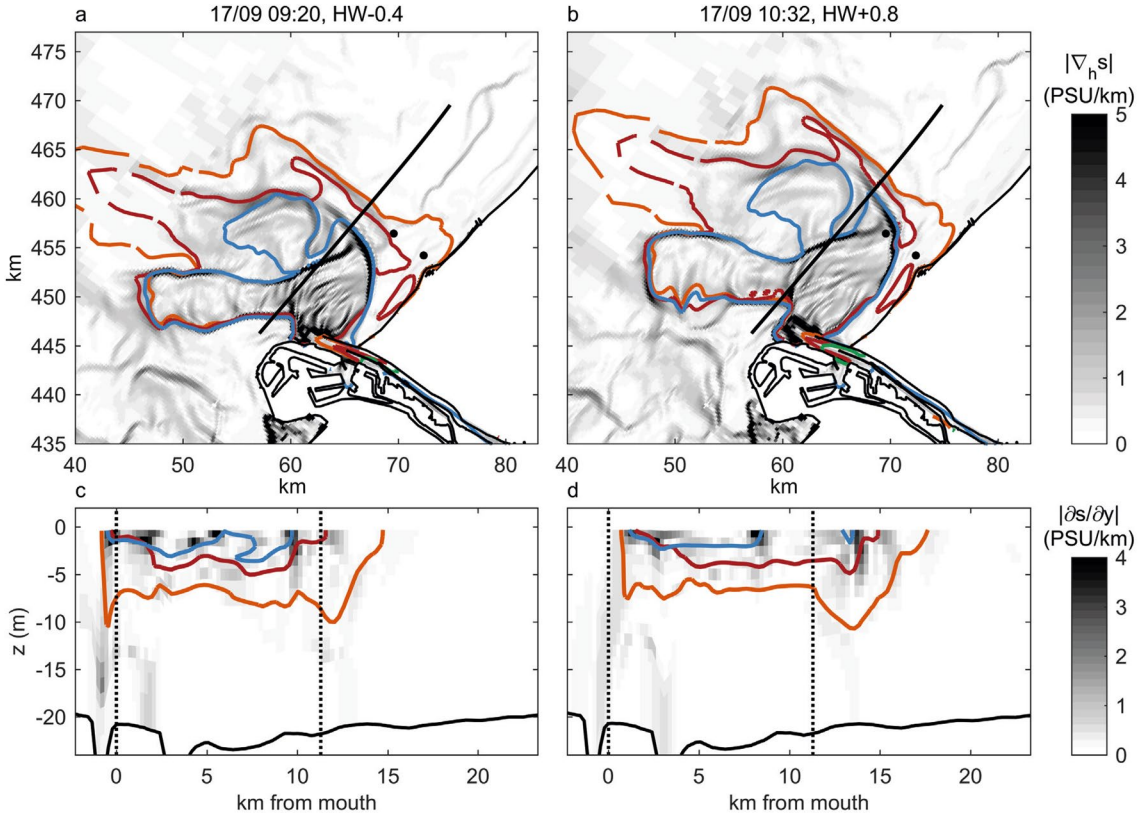

Figure 12. (a and b) Plan view of horizontal salinity gradient (PSU/km), (c and d) cross-section of salinity gradient in alongshore direction (PSU/km), both with contour lines of four tracers, for a neap tide at HW−0.4 and HW+0.8 h (day 260 or 17/09). The solid colored lines in panels a and b correspond to the 85% contour line of the plan view (surface). The solid lines in c and d, correspond to the 85% contour line of the cross-section. The four colors represent the different tracers: orange is tracer 1, red is tracer 2, blue is tracer 3 and green is tracer 4. Tracer 3 corresponds to Figures 8g–8i. The black line in panels a and b is the cross-section in panels c–h. The vertical dotted lines correspond to the location of the river mouth and the mooring stations. The horizontal and vertical axes in panels a and b are displayed in RD coordinates in km.

frontal strength, $\frac{\partial s}{\partial n}$, for one neap and spring tidal cycle. The selected neap and spring event corresponds to the same tidal cycle shown in Figures 8–10, 12 and 13.

The frontogenesis terms are shown for two frontal trajectories in Figure 14: The downstream edge of the plume that propagates parallel to the coast, the coastal edge of the plume that turns and propagates into the coast (see yellow dots in Figure 10). The front is strongest around 2–3 h since LW and then strengthens a second time around 9–9.5 h since LW for neap and 6.5 h for spring (Figures 14 and 15). This is true for the downstream and coastal trajectories.

The first peak occurs during the transition from ebb to flood tide and is clearest on the downstream frontal boundary for both the neap and spring tide (Figures 14d, 14g, 15c, and 15e). The front is formed by the ebb-tidal plume after it has been discharged from the river mouth and begins to propagate downstream up the coast (Figure 10). The strength of the front peaks again during flow reversal from flood to ebb for neap and a bit earlier for the spring tidal cycle. On the coastal boundary the second peak is more than twice as high as on the downstream boundary and twice as high as the first peak for neap. For spring, the second peak is actually higher on the downstream front.

The frontogenesis analysis confirms that both peaks are associated with strong cross-frontal convergence $\frac{\partial u}{\partial n}\frac{\partial s}{\partial n}$, with secondary contributions from the twisting term $\frac{\partial v}{\partial n}\frac{\partial s}{\partial p}$ (Figures 14g, 14h and 15e–15f). Convergence in TPFs is driven by advection of buoyant estuary water over ambient coastal water, as described in previous plume frontal studies (Kilcher & Nash, 2010; Luketina & Imberger, 1987).

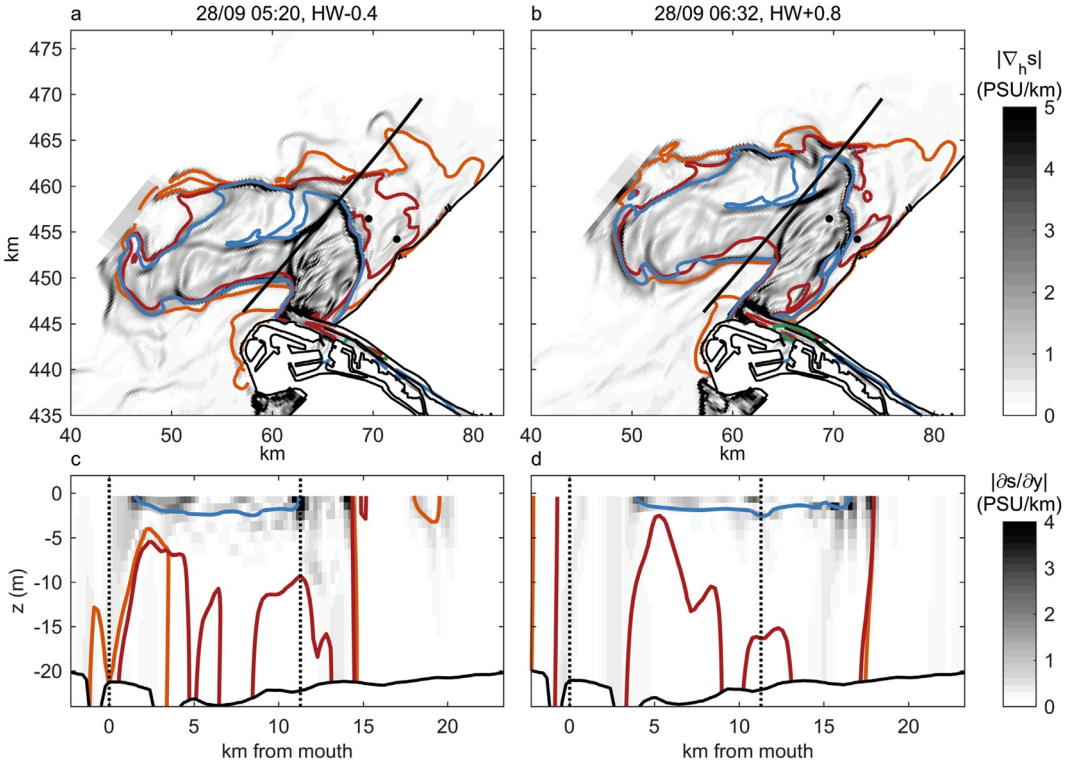

Figure 13. (a and b) Plan view of horizontal salinity gradient (PSU/km), (c and d) cross-section of salinity gradient in alongshore direction (PSU/km), both with contour lines of four tracers, for a spring tide at HW−0.4 and HW+0.8 h (day 271 or 28/09). Tracer 3 (blue) corresponds to Figures 9g–9i. Same description as Figure 12.

The second peak, however, occurs well after the estuary outflow has lost its initial inertia and must be explained by another mechanism. Comparison with results from de Boer et al. (2006, 2008) shows that the timing of this peak coincides approximately with the peak in the vertical shear within the plume resulting from cross-shore tidal straining. Therefore, we estimated cross-shore tidal straining, S_x, ahead and behind the front (Figures 14j, 14k and 15g–15h). At the time of the second peak, tidal straining behind the front, within the stratified tidal plume, is larger than ahead of the front. This results in an enhanced onshore flow in the upper plume layer compared to the stratified coastal waters. This process enhances frontal convergence as coastal water is forced under the onshore propagating plume, as observed in the frontogenesis analysis (Figures 14g, 14h and 15e–15f). So, cross-shore tidal straining seems to be able to re-strengthen the TPFs.

Along the coastal boundary of the front, flow may also be displaced alongshore and the front propagates toward the coast. Together with the enhancement of rotational tidal flow associated with strong stratification in the plume this process appears to increase the magnitude of the twisting term. The twisting term strengthens the front as the along-front velocity shear differentially advects buoyancy along the front and increases the cross-front density gradient.

We also observe that weak gradients that survive long after a front has lost its initial strength may be re-strengthened. An example of this process is shown in Figures 14c, 14f, 14i, and 14l for a front that was formed one tidal cycle beforehand. Figures 16b–16f shows the trajectory (red dot and line) and cross-sectional view of that front for six hours. We anticipate that tidal straining may strengthen these relic fronts if stratification is stronger on one side than the other. This effect is swamped for the front considered in Figures 14c, 14f, 14i and 14l. which re-strengthens as a newer front overtakes it. The process by which one front overtakes and absorbs another will not be studied in detail here, though it may be that the convergent circulation of the younger front acts on the gradient of the relic front in such a way that it re-sharpens.

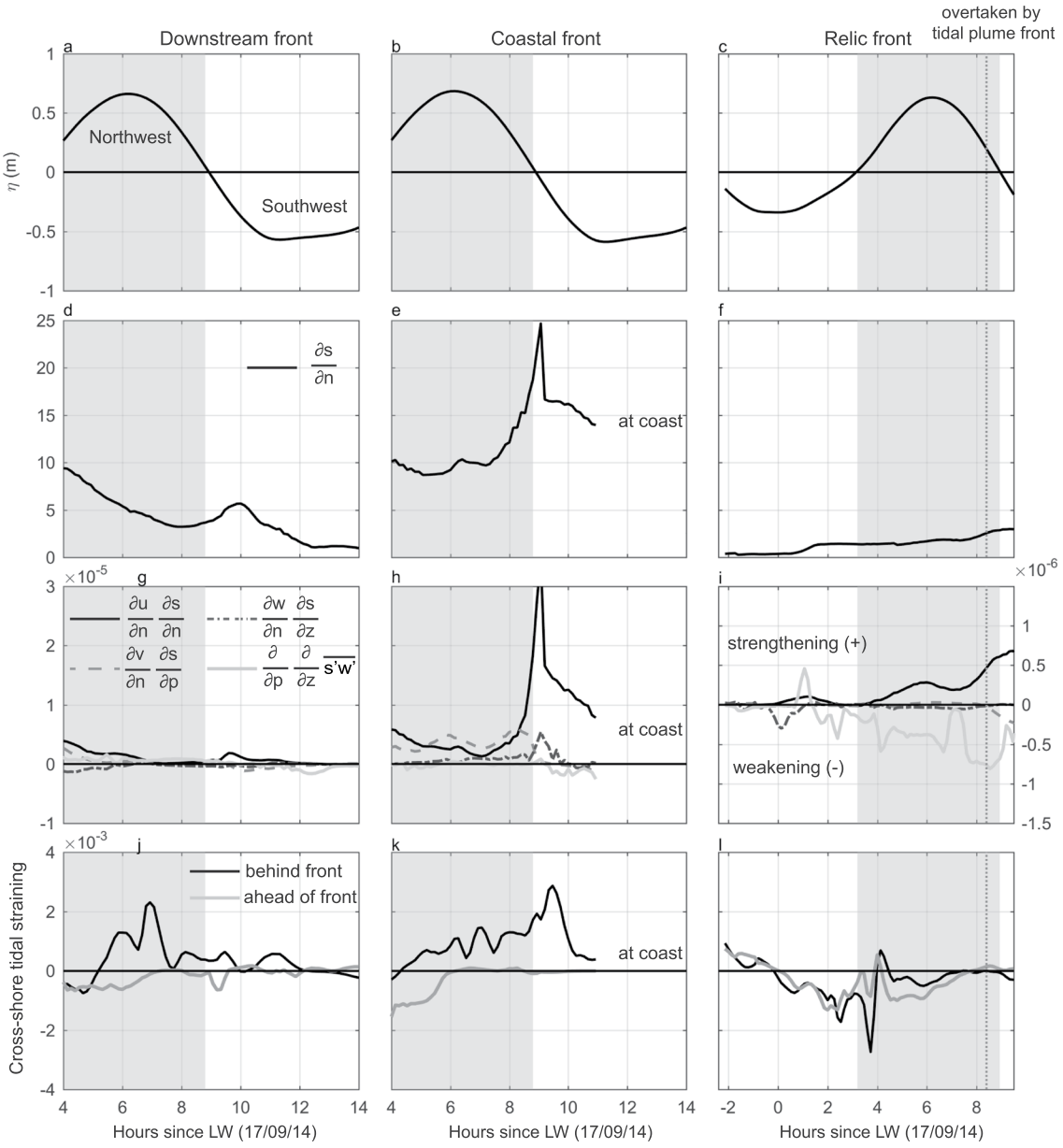

Figure 14. Lagrangian frontogenesis analysis using three front trajectories on day 17/09/2014 (neap tide). The first two columns represent two trajectories on the shown in Figures 11a by the yellow dots. The third column represents a trajectory on a relic front, which is visible in Figure 16. (a–c) Tidal elevation in meters, panels (d–f) front normal gradient, (g–i) RHS frontogenesis terms in $m^{-1}s^{-1}$ (see Equation 5). Positive values indicate strengthening the front, while negative values indicate weakening of the front. (j–l) Cross-shore tidal straining terms ahead and behind the front in Wm^{-3}, the gray and black line respectively. The southern trajectory (b, e, h, and k) hits the Sand Engine around 14:40 (11 h since low water (LW)) and stays attached to the coastline until 18:00 (13.9 h since LW). The dotted vertical line is the time when the TPF overtakes the relic front. The subscripts *n* and *p* refer to front normal and front parallel. Note that panel i has different *y*-axis limits (on the right) than panels g and h.

The analysis of the downstream and coastal frontal boundaries indicates that mixing contributes to weakening of the front. This is evidenced by the negative values of the mixing term after the second peak (Figures 14g and 14h). However, the frontal strength decreases well below its peak value one to two hours before the observed mixing begins and the strength of the front appears instead to follow the increase and decrease in convergence closely. This suggests that frontal strength is determined primarily by the increases and decreases in convergence associated with the plume dynamics and that mixing plays a secondary role. This observation is consistent with the model-estimated eddy viscosity (Figures 16g and 16h), which shows modest

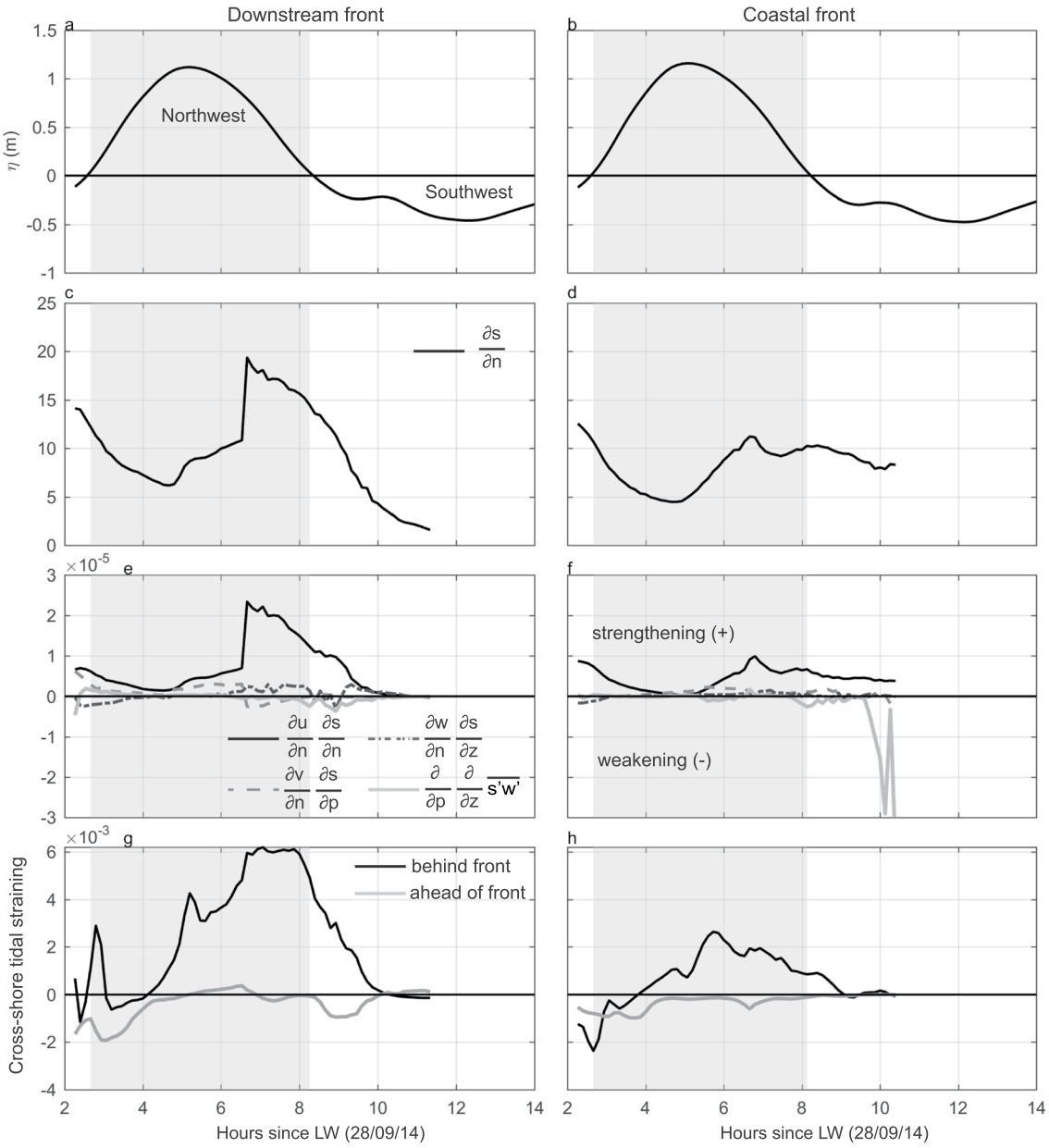

Figure 15. Lagrangian frontogenesis analysis using two front trajectories on day 28/09/2014 (spring tide). The two columns represent two trajectories on the tidal plume front shown in Figure 10b by the yellow dots. (a–b) Tidal elevation in meters, panels (c–d) front normal gradient, (e–f) RHS frontogenesis terms in $m^{-1}s^{-1}$ (see Equation 5). Positive values indicate strengthening the front, while negative values indicate weakening of the front. (g–h) Cross-shore tidal straining terms ahead and behind the front in Wm^{-3}, the gray and black line respectively. The subscripts *n* and *p* refer to front normal and front parallel.

peaks at the tidal plume and relic fronts but is generally low relative to the bottom boundary turbulence. Of course, caution must be taken when interpreting turbulence results at a front with a hydrostatic model.

5. Discussion

5.1. Multiple Plume Fronts

The model simulations and the mooring data provide a conceptual picture of the frontal structure in the Rhine ROFI. This multiple front system is generated by different processes, where depth-mean advection, tidal straining (differential advection), convergence, and mixing all play important roles. Every tidal cycle

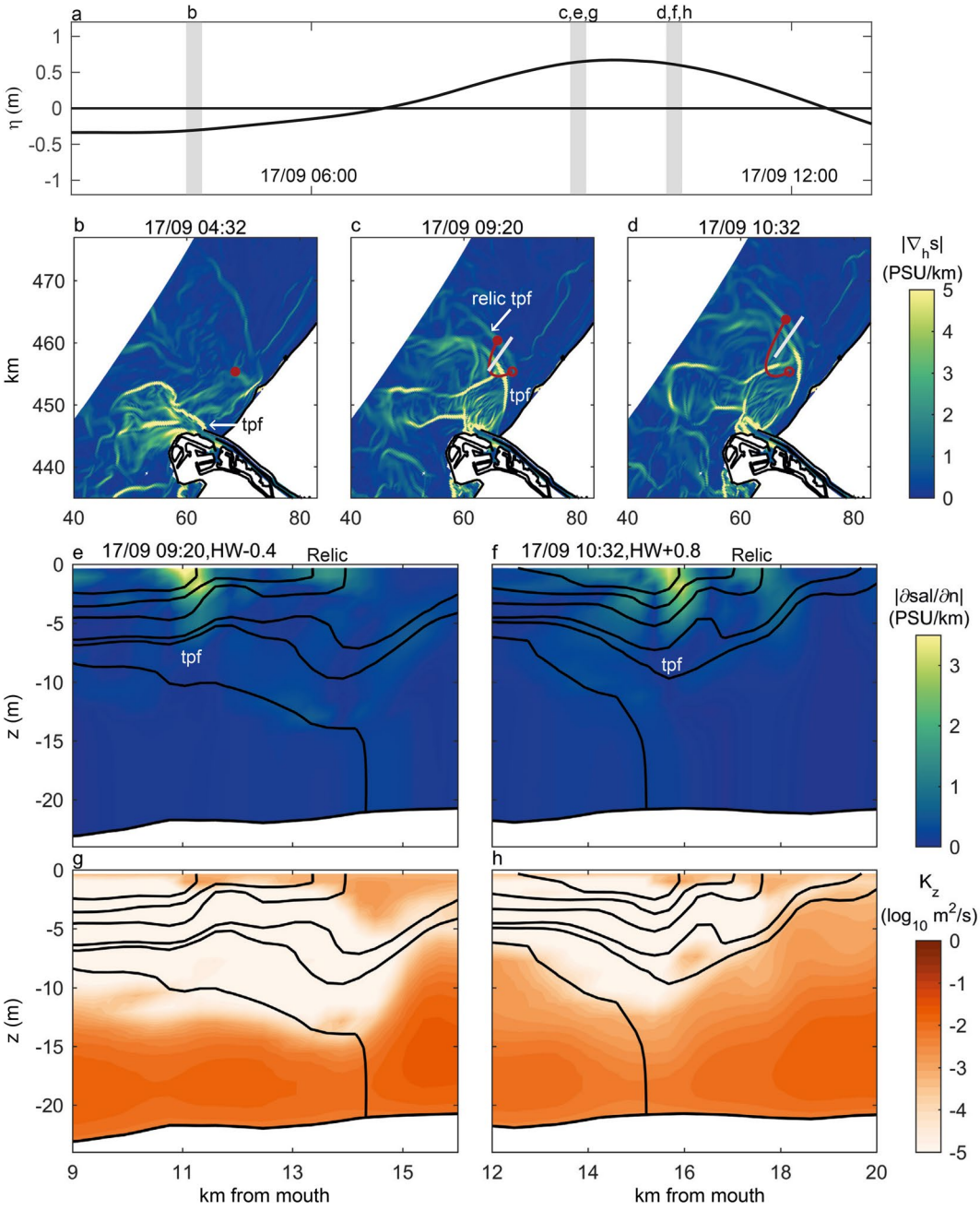

Figure 16. (a) Tidal elevation showing the location of each panel in time. (b–d) Plan view of the total horizontal salinity gradient at the surface (PSU/km) at three different times. Panel (b) is during the first ebb on September 17, 2014, panels (c–d) are during the consecutive flood. (e–h) Transects across the tidal plume front (TPF) and a relic TPF (relic) along the cross-section indicated in panels c and d for HW−0.4 and HW+0.8 h (e–f) salinity gradient along the cross-section (alongshore; PSU/km), (g–h) vertical eddy viscosity (log10 m^2/s). The black lines represent salinity contours of 27, 28, 28.9, 29.6, 29.8, and 30.3 PSU. The red dots (b–d) mark a location on the relic front. The trajectory of this front is shown by the red line. The red circle (c–d) refers to the starting point of the trajectory back in time.

a TPF is formed at the river mouth and propagates down the coast at a speed set by its intrinsic speed and the coastal tidal velocity. As the tidal forcing is relaxed and stratification increases, the tidal currents become more elliptical carrying the TPF in an elliptical pathway. The front gets weaker as the flood velocities weaken and then re-strengthens around the time of the flood-to-ebb transition. In some cases the fronts are observed to persist well into the next tidal cycle. These relic fronts are weak, with much lower cross-frontal

density gradients, but can also re-strengthen due to tidal straining or when they are overtaken and absorbed into newer fronts. Over one to two tidal cycles the ebb tidal plume water is absorbed into the existing coastal plume water and forms the background plume stratification. At the same time, the tidal currents are modified in the presence of this stratification and generate along- and cross-shore tidal straining, which leads to the on- and offshore movement of the IF of the ROFI each tidal cycle.

Our findings suggest that the longevity of the TPFs in this system is larger than one tidal cycle resulting in a multi-frontal system, which is inline with the Sentinel image (Figure 1b) and the field-data (Figures 6a–6d). The use of remote sensing and model simulations helps to differentiate between the different fronts, as data from moored instrumentation will not give us definite information on the nature of a front. The density signal in Figures 6a–6d shows clearly the presence of the TPF (roman numbers) and relic TPFs (black cross). Relic tidal plume water is observed in other river plume systems such as the Columbia River plume as well, where it influences the new TPFs (Horner-Devine et al., 2009; Kilcher & Nash, 2010).

5.2. Do the Tidal Plume Fronts Interact?

We found that fronts move inside the tidal plume, while de Ruijter et al. (1997) suggested separate pulses (blobs) moved along the coast. This difference may be attributed to the different weather conditions and mixing regimes experienced in the two studies. Here we only investigate a relatively calm neap and spring period. The numerical tracers demonstrate that the different fronts move and spread within the tidal plume, where the newest front seems to move faster than older relic fronts (Figures 12, 13 and 16). Bottom tidal mixing influences the structure of the different plumes and fronts by vertical mixing and inhibiting spreading, resulting in a different relic tidal plume structure between neap and spring. Based on our findings, we hypothesize that the observed TPFs and relic fronts interact with each other as they spread; as a result, newer fronts can overtake and coalesce with slower ones. The detailed dynamics of this interaction are three-dimensional and too complex to resolve with the hydrostatic model.

Another difference with the observations in de Ruijter et al. (1997) is the port extension next to the river mouth, which was completed in December 2013 (Figure 1). This reclamation of this 8 km by 5–6 km area could potentially impact the flow field, and several studies have shown that reclamations into the sea can generate eddies (Davies et al., 1990; Geyer, 1993; Magaldi et al., 2008; Signell & Geyer, 1991). A large recirculation, with a diameter of roughly 10–20 km, is indeed observed downstream of the river mouth between HW+2 and HW+4 (Figures 7–9, Supporting Information Movies S1 and S2). This eddy may be associated with the bulge circulation observed in many river plumes, generated by the port extension or may be a combination of both processes. We observe the eddy only during a period of 60–90 min, coinciding with the period of onshore tidal currents, and only in the upper layer. This suggests that this eddy is due to the interaction of multiple processes, including elliptical tidal currents. Examination of the movies (Supporting Information) shows that the presence of this eddy has an impact on the pathway of the fronts and appears to play a role in retaining them in the mid-field region of the plume.

5.3. Strengthening of Tidal Plume Fronts

The Lagrangian frontogenesis equation (Equation 5) clearly shows that there is strong convergence when the front is strong and it weakens as the frontal strength diminishes. Frontal mixing and twisting appear to be secondary processes. Figures 14 and 15 suggest that the strength of the front and the related convergence depends on the external plume dynamics. It appears that tidal straining plays an important role in enhancing convergence and hence the fronts. The TPF is enhanced when it starts to propagate northeastwards after the first ebb to flood reversal. At this point the front travels along shore much faster than the ambient water, increasing convergence at the downstream front and the coastal front (Figure 14). There is a second enhancement of the frontal strength and convergence around the high water to low water flow reversal. This is also the moment when tidal straining is large. Figures 14 and 15 suggest that this enhancement is driven by tidal straining. Figure 17 tries to explain this mechanism. Thus, the strong ellipticity of the tides appears to be important in enhancing the fronts. Another clear sign of the influence of the coastal convergence is that the twisting component also increases (Figure 14). Similar dynamics are observed with the relic fronts, with maximum frontal strength and convergence around flow reversal, although the relic front could be

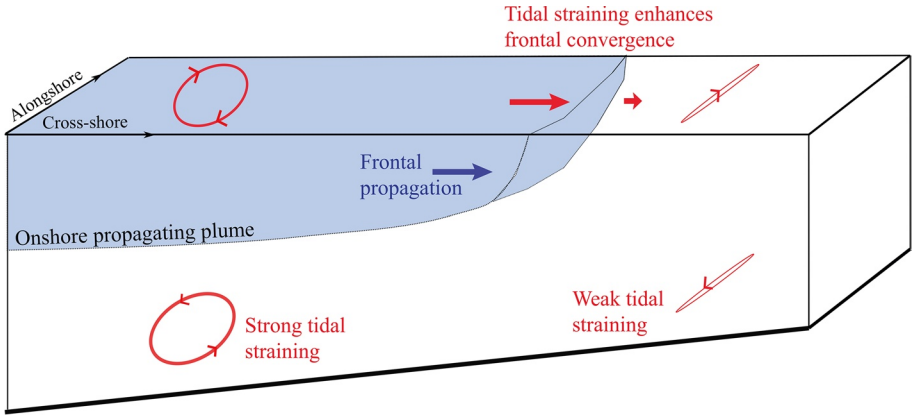

Figure 17. Schematic explaining the enhancement of frontal strength by the presence of tidal straining. Red corresponds to the effect of tidal straining and blue to the fronts. The ellipses indicate the counter rotating surface and bed currents responsible for the presence of tidal straining.

momentarily enhanced when the new front catches up, before overtaking it. Previous studies showed that tidal straining is very small in the downstream plume during spring tides (de Boer et al., 2006; Simpson & Souza, 1995). However, Figure 15 suggests that this process is present in the tidal plume, and plays an important role in re-strengthening the fronts by generating cross-shore convergence.

The frontogenesis analysis together with the tracers demonstrate that stratification and currents in the ambient coastal waters play an important role in this multi-frontal system. The front trajectories show indeed that the Rhine TPFs are controlled by tidal straining and tidal advection, resulting in an elliptical pathway each tidal cycle (Figure 10). The dominant role of the tidal straining leads to the trapping of the fronts within a radius of roughly 20 km from the river mouth (Figures 12 and 13). The traveled distance of the fronts per tidal cycle seems to align with the tidal excursion length, indicating the importance of tidal advection. We obtain a tidal excursion length of 15 km based on a maximum tidal velocity of 1 m/s and on the M2 tidal frequency.

We anticipate that the frontal trapping observed in the Rhine ROFI may be explained in part by the ratio of the intrinsic frontal speed and the ambient tidal current. The intrinsic frontal speed is two times smaller than the ambient tidal currents based on field measurements (Rijnsburger et al., 2018a). This characteristic frontal dynamics in the Rhine ROFI seems to be somewhat different than in other systems, where smaller ambient tidal currents are observed. One example is the Columbia River plume where the intrinsic frontal speed is three times larger than the ambient coastal currents, based on mean values of 0.6 ms^{-1} (Kilcher & Nash, 2010) and 0.2 ms^{-1} (Garcí a Berdeal et al., 2002; Hickey et al., 1998, 2005). This gives a ratio of $u_f/u_0 \approx 3$, while the Rhine River plume has a ratio of u_f/u_0 0.5/1 ≈ 0.5. This analysis suggests that TPFs can outrun tidal currents in the Columbia plume, but that they may be trapped in the Rhine plume.

The trapping poses the following question: How is freshwater from the tidal plumes transported into the far-field when the fronts are kept within 20 km of the river mouth? To address this we calculated the total mass of tracer concentration transported into the far-field compared to the total mass present in the entire river plume. We set the boundary to the far-field as a cross-shore section located roughly 18 km downstream of the river mouth and extending over the entire model domain. After five tidal cycles, approximately 30% and 10% of the tracer concentration is located in the far-field for neap and spring respectively. These numbers suggest that roughly three times as much water is transported into the far-field for the neap as for the spring. Vertical tidal mixing is larger during spring tides (Rijnsburger et al., 2018a; Simpson & Souza, 1995), leading to vertically mixed tracer concentration after 2 tidal cycles, in contrast to the neap tide when dispersion appears to be dominant in the horizontal direction (see Supporting Information Movies S3 and S4). Hence, a balance between the horizontal salinity gradients, tidal mixing and tidal advection is expected to determine the alongshore transport.

5.4. Limitations

It should be noted that the TPFs are inherently non-hydrostatic. However, non-hydrostatic three-dimensional numerical models are computationally challenging to use. Therefore, we use a three-dimensional hydrostatic model to study frontal propagation and evolution. In a hydrostatic model the vertical velocity is obtained from the continuity equation, therefore vertical accelerations are not directly calculated. As a result, the model will not resolve the small-scale non-hydrostatic features of the fronts, but only estimates the larger scale properties such as propagation speed, direction, and corresponding horizontal salinity gradients. Several studies show that hydrostatic models are useful for understanding the bulk properties of fronts (Cole et al., 2020). In this study, the front properties and trajectories are reasonable, but in-depth study of frontal evolution is left over for future work with a non-hydrostatic model.

Moreover, regions with sharp gradients, such as the fronts explored here, are difficult to simulate numerically. Upstream based advection schemes are known to suffer from numerical diffusion, while even ordered central schemes suffer from numerical dispersion, which can be controlled with limiters, see for example, Pietrzak (1998). Typically, similar higher order advection schemes are used in ocean models, with limiters, for example, GETM (Burchard et al., 2004). In DELFT3D a combination of second order and third order differences is applied, where the numerical diffusion, from the third order scheme, acts to damp the over and under shoot from the second order scheme, but does not guarantee a monotone solution (Deltares, 2019). In addition we use the k-ε turbulence closure scheme for vertical mixing. No attempt was made to calibrate the coefficients. See Fringer et al. 2019 for a summary of the limitations commonly found in ocean models when simulating fronts.

The frontal trajectories used here are based on a Lagrangian tracking method that relies on the surface velocity instead of horizontal salinity gradients. The velocity follows the salinity gradients relatively well, however, some offset could be induced due to the complex velocity field around the fronts. This could lead to a slight offset in position compared to the highest gradient. Additionally, in this system the fronts rotate due to the tidal current and are not straight lines, complicating the determination of cross- and along-front direction.

6. Conclusions

A 3D numerical model has allowed us to interpret in-situ measurements and develop a conceptual picture of the frontal structure in the Rhine ROFI. The horizontal salinity gradient and numerical tracers have shown to be a useful tool to identify three types of front: IFs, TPFs and relic fronts. The combination of salinity gradients and numerical tracers showed that TPFs can be sustained for longer than one tidal cycle, eventually becoming relic TPFs. We find that tidal straining can play an important role in strengthening fronts: Straining generates more vertical shear within the stratified plume compared with weakly stratified ambient waters, resulting in increased convergence at the front and increasing frontal strength. We observe that this process re-strengthens the TPF during neap and spring tide, with a difference in time. During neap tides this process seems to be strongest at the flood ebb reversal, while during spring this occurs earlier. Re-strengthening of the TPFs could explain the presence of relic fronts in the Rhine ROFI. As the Rhine ROFI is a strong tidally energetic system, we observe that the frontal dynamics are controlled mainly by the external forces; the strength and propagation of the fronts are controlled by tidal straining and advection processes and the degree of stratification in ambient coastal waters, which is determined by tidal mixing. In addition, the frontogenesis analysis shows that frontal mixing, twisting and stretching are secondary forcings. We believe that the presence of multiple fronts will likely change the transport patterns, cross-shore exchange and stratification in the river plume, which are key processes for ecosystem health, water quality and coastal erosion.

Data Availability Statement

The field- and numerical data used in this paper are published as data sets in the 4TU Center for Research Data in the Netherlands (Rijnsburger et al., 2018b; Rijnsburger et al., 2021).

Acknowledgments
The project is funded by the Netherlands Technology Foundation STW program project Sustainable engineering of coastal systems in Regions of Freshwater Influence (project 12682), awarded to J.D. Pietrzak and H.J.H. Clercx. R. P. Flores would like to thank the Fulbright Commission and CONICYT-Chile for the scholarship provided. ARH-D was supported by the Allan and Inger Osberg Professorship. A. J. Souza was funded by NERC through NOC National Capability funding. The authors would like to thank Deltares and the Port of Rotterdam for their support on the Delft3D model; the crew of the R.V. Zirfea, Martijn Henriquez, Saulo Mereilles, Margaret McKeon, Richard Cooke, Christopher Balfour and Rijkswaterstaat for their valuable contribution during collection of the field-data; Hugo Platell for sharing his knowledge and code on the Taylor Goldstein Equation; and Stef Lhermitte for providing the Sentinel-1 image.

References

Akan, Ç., McWilliams, J. C., Moghimi, S., & Özkan-Haller, H. T. (2018). Frontal dynamics at the edge of the Columbia River plume. *Ocean Modelling*, *122*, 1–12. https://doi.org/10.1016/j.ocemod.2017.12.001

Benjamin, T. B. (1968). Gravity currents and related phenomena. *Journal of Fluid Mechanics*, *31*, 209–248. https://doi.org/10.1017/s0022112068000133

Britter, R., & Simpson, J. (1978). Experiments on the dynamics of a gravity current head. *Journal of Fluid Mechanics*, *88*, 223–240. https://doi.org/10.1017/s0022112078002074

Brown, J. M., Norman, D. L., Amoudry, L. O., & Souza, A. J. (2016). Impact of operational model nesting approaches and inherent errors for coastal simulations. *Ocean Modelling*, *107*, 48–63. https://doi.org/10.1016/j.ocemod.2016.10.005

Burchard, H., Bolding, K., & Villarreal, M. R. (2004). Three-dimensional modeling of estuarine turbidity maxima in a tidal estuary. *Ocean Dynamics*, *54*(2), 250–265. https://doi.org/10.1007/s10236-003-0073-4

Cole, K. L., MacDonald, D. G., Kakoulaki, G., & Hetland, R. D. (2020). River plume source-front connectivity. *Ocean Modelling*, *150*, 1–11. https://doi.org/10.1016/j.ocemod.2020.101571

Cromwell, T., & Reid, J. L., Jr. (1956). A Study of Oceanic Fronts. *Tellus*, *8*, 94–101. https://doi.org/10.3402/tellusa.v8i1.8947

Davies, P. A., Davis, R. G., & Foster, M. R. (1990). Flow past a circular cylinder in a rotating stratified fluid. *Philosophical Transactions of the Royal Society A: Mathematical, Physical and Engineering Sciences*, *331*, 245–286. https://doi.org/10.1098/rsta.1990.0066

de Boer, G. J., Pietrzak, J. D., & Winterwerp, J. C. (2006). On the vertical structure of the Rhine region of freshwater influence. *Ocean Dynamics*, *56*, 198–216. https://doi.org/10.1007/s10236-005-0042-1

de Boer, G. J., Pietrzak, J. D., & Winterwerp, J. C. (2007). SST observations of upwelling induced by tidal straining in the Rhine ROFI. *Continental Shelf Research*, *29*, 263–277. https://doi.org/10.1016/j.csr.2007.06.011

de Boer, G. J., Pietrzak, J. D., & Winterwerp, J. C. (2008). Using the potential energy anomaly equation to investigate tidal straining and advection of stratification in a region of freshwater influence. *Ocean Modelling*, *22*, 1–11. https://doi.org/10.1016/j.ocemod.2007.12.003

de Kok, J. (1997). Baroclinic eddy formation in a Rhine plume model. *Journal of Marine Systems*, *12*, 35–52. https://doi.org/10.1016/s0924-7963(96)00087-5

Deltares (2014). Delft3D-Flow User Manual (Vol. 3.15; *Tech. Rep.*). Delft, The Netherlands.

Deltares (2019). Delft3D-Flow user manual *Version 3.15*. Delft.

de Nijs, M. A., & Pietrzak, J. D. (2012). Saltwater intrusion and ETM dynamics in a tidally-energetic stratified estuary. *Ocean Modelling*, *49–50*, 60–85. https://doi.org/10.1016/j.ocemod.2012.03.004

de Ruijter, W. P., Visser, A. W., & Bos, W. (1997). The Rhine outflow: A prototypical pulsed discharge plume in a high energy shallow sea. *Journal of Marine Systems*, *12*, 263–276. https://doi.org/10.1016/s0924-7963(96)00102-9

Fischer, E., Burchard, H., & Hetland, R. D. (2009). Numerical investigations of the turbulent kinetic energy dissipation rate in the Rhine region of freshwater influence. *Ocean Dynamics*, *59*, 629–641. https://doi.org/10.1007/s10236-009-0187-4

Flores, R. P. (2018). The dynamics of cross-shore sediment transport in the Rhine region of freshwater influence (Doctoral dissertation, University of Washington). Retrieved from http://hdl.handle.net/1773/43006

Flores, R. P., Rijnsburger, S., Horner-Devine, A. R., Souza, A. J., & Pietrzak, J. D. (2017). The impact of storms and stratification on sediment transport in the Rhine region of freshwater influence. *Journal of Geophysical Research: Oceans*, *122*, 4456–4477. https://doi.org/10.1002/2016jc012362

Fong, D. A., Geyer, W., & Signell, R. (1997). The wind-forced response on a buoyant coastal current: Observations of the western Gulf of Maine plume. *Journal of Marine Systems*, *12*, 69–81. https://doi.org/10.1016/s0924-7963(96)00089-9

Fong, D. A., & Geyer, W. R. (2001). Response of a river plume during an upwelling favorable wind event. *Journal of Geophysical Research*, *106*, 1067–1084. https://doi.org/10.1029/2000jc900134

Fringer, O. B., Dawson, C. N., He, R., Ralston, D. K., & Zhang, Y. J. (2019). The future of coastal and estuarine modeling: Findings from a workshop. *Ocean Modelling*, *143*, 101458. https://doi.org/10.1016/j.ocemod.2019.101458

García Berdeal, I., Hickey, B. M., & Kawase, M. (2002). Influence of wind stress and ambient flow on a high discharge river plume. *Journal of Geophysical Research*, *107*(C9), 3130. https://doi.org/10.1029/2001jc000932

Garvine, R. W. (1974). Physical features of the Connecticut River outflow during high discharge. *Journal of Geophysical Research*, *79*, 831–846. https://doi.org/10.1029/jc079i006p00831

Garvine, R. W. (1984). Radial spreading of buoyant, surface plumes in coastal waters. *Journal of Geophysical Research*, *89*, 1989–1996. https://doi.org/10.1029/jc089ic02p01989

Garvine, R. W. (1995). A dynamical system for classifying buoyant coastal discharges. *Continental Shelf Research*, *15*, 1585–1596. https://doi.org/10.1016/0278-4343(94)00065-u

Garvine, R. W., & Monk, J. D. (1974). Frontal structure of a river plume. *Journal of Geophysical Research*, *79*, 2251–2259. https://doi.org/10.1029/jc079i015p02251

Geyer, W. R. (1993). Three-dimensional tidal flow around headlands. *Journal of Geophysical Research*, *98*, 955–966. https://doi.org/10.1029/92jc02270

Geyer, W. R., & Ralston, D. K. (2015). Estuarine frontogenesis. *Journal of Physical Oceanography*, *45*, 546–561. https://doi.org/10.1175/jpo-d-14-0082.1

Giddings, S. N., Fong, D. A., Monismith, S. G., Chickadel, C. C., Edwards, K. A., Plant, W. J., et al. (2012). Frontogenesis and frontal progression of a trapping-generated estuarine convergence front and its influence on mixing and stratification. *Estuaries and Coasts*, *35*, 665–681. https://doi.org/10.1007/s12237-011-9453-z

Hessner, K., Rubino, A., Brandt, P., & Alpers, W. (2001). The Rhine outflow plume studied by the analysis of synthetic aperture radar data and numerical simulations. *Journal of Physical Oceanography*, *31*, 3030–3044. https://doi.org/10.1175/1520-0485(2001)031<3030:tropsb>2.0.co;2

Hetland, R. D. (2005). Relating river plume structure to vertical mixing. *Journal of Physical Oceanography*, *35*, 1667–1688. https://doi.org/10.1175/jpo2774.1

Hickey, B., Geier, S., Kachel, N., & MacFayden, A. (2005). A bi-directional river plume: The Columbia in summer. *Continental Shelf Research*, *25*, 1631–1656. https://doi.org/10.1016/j.csr.2005.04.010

Hickey, B., Kudela, R. M., Nash, J. D., Bruland, K. W., Peterson, W. T., MacCready, P., & Lohan, M. C. (2010). River influences on shelf ecosystems: Introduction and synthesis. *Journal of Geophysical Research*, *115*, 1–26. https://doi.org/10.1029/2009jc005452

Hickey, B., Pietrafesa, L., Jay, D., & Boicourt, W. (1998). The Columbia River plume study: Subtidal variability in the velocity and salinity fields. *Journal of Geophysical Research*, *103*, 10339–10368. https://doi.org/10.1029/97jc03290

Horner-Devine, A. R., Chickadel, C. C., & MacDonald, D. G. (2013). Coherent structures and mixing at a river plume front. In J. G. Venditti, J. L. Best, M. Church, & R. J. Hardy (Eds.), *Coherent flow structures at earth's surface*. Chichester, UK. John Wiley & Sons.

Horner-Devine, A. R., Hetland, R. D., & MacDonald, D. G. (2015). Mixing and transport in coastal river plumes. *Annual Review of Fluid Mechanics*, *47*, 569–594. https://doi.org/10.1146/annurev-fluid-010313-141408

Horner-Devine, A. R., Jay, D. A., Orton, P. M., & Spahn, E. Y. (2009). A conceptual model of the strongly tidal Columbia River plume. *Journal of Marine Systems*, *78*, 460–475. https://doi.org/10.1016/j.jmarsys.2008.11.025

Horner-Devine, A. R., Pietrzak, J. D., Souza, A. J., Mckeon, M. A., Meirelles, S., Henriquez, M., et al. (2017). Cross-shore transport of nearshore sediment by river plume frontal pumping. *Geophysical Reseach Letters*, *44*, 6343–6351. https://doi.org/10.1002/2017gl073378

Jay, D. A., Pan, J., Orton, P. M., & Horner-Devine, A. R. (2009). Asymmetry of Columbia River tidal plume fronts. *Journal of Marine Systems*, *78*, 442–459. https://doi.org/10.1016/j.jmarsys.2008.11.015

Kabat, P., Fresco, L. O., Stive, M. J. F., Veerman, C. P., van Alphen, J. S. L. J., Parmet, B. W. A. H., et al. (2009). Dutch coasts in transition. *Nature Geoscience*, *2*, 450–452. https://doi.org/10.1038/ngeo572

Kilcher, L. F., & Nash, J. D. (2010). Structure and dynamics of the Columbia River tidal plume front. *Journal of Geophysical Research*, *115*, 1–20. https://doi.org/10.1029/2009jc006066

Lesser, G. R., Roelvink, J. A., van Kester, J. A., & Stelling, G. S. (2004). Development and validation of a three-dimensional morphological model. *Coastal Engineering*, *51*, 883–915. https://doi.org/10.1016/j.coastaleng.2004.07.014

Luketina, D. A., & Imberger, J. (1987). Characteristics of a surface buoyant jet. *Journal of Geophysical Research*, *92*, 5435–5447. https://doi.org/10.1029/jc092ic05p05435

Magaldi, M. G., Özgökmen, T. M., Griffa, A., Chassignet, E. P., Iskandarani, M., & Peters, H. (2008). Turbulent flow regimes behind a coastal cape in a stratified and rotating environment. *Ocean Modelling*, *25*, 65–82. https://doi.org/10.1016/j.ocemod.2008.06.006

Marmorino, G. O., & Trump, C. L. (2000). Gravity current structure of the Chesapeake Bay outflow plume. *Journal of Geophysical Research*, *105*, 28847–28861. https://doi.org/10.1029/2000jc000225

Nash, J. D., & Moum, J. N. (2005). River plumes as a source of large-amplitude internal waves in the coastal ocean. *Nature*, *437*, 400–403. https://doi.org/10.1038/nature03936

Nicholls, R. J., & Cazenave, A. (2010). Sea level rise and its impact on coastal zones. *Science*, *328*, 1517–1520. https://doi.org/10.1126/science.1185782

O'Donnell, J. (1988). A numerical technique to incorporate frontal boundaries in two-dimensional layer models of ocean dynamics. *Journal of Physical Oceanography*, *18*, 1584–1600.

O'Donnell, J. (1990). The formation and fate of a river plume: A numerical model. *Journal of Physical Oceanography*, *20*, 551–569. https://doi.org/10.1175/1520-0485(1990)020<0551:TFAFOA>2.0.CO;2

O'Donnell, J. (1993). Surface fronts in estuaries: A review. *Estuaries*, *16*, 12–39.

O'Donnell, J., Ackleson, S. G., & Levine, E. R. (2008). On the spatial scales of a river plume. *Journal of Geophysical Research*, *113*, 1–12. https://doi.org/10.1029/2007JC004440

O'Donnell, J., Marmorino, G. O., & Trump, C. L. (1998). Convergence and downwelling at a river plume front. *Journal of Physical Oceanography*, *28*, 1481–1495. https://doi.org/10.1175/1520-0485(1998)028<1481:CADAAR>2.0.CO;2

Orton, P. M., & Jay, D. A. (2005). Observations at the tidal plume front of a high-volume river outflow. *Geophysical Research Letters*, *32*, 1–4. https://doi.org/10.1029/2005gl022372

Pietrzak, J. (1998). The use of TVD limiters for forward-in-time upstream-biased advection schemes in ocean modeling. *Monthly Weather Review*, *126*(3), 812–830. https://doi.org/10.1175/1520-0493(1998)126<0812:TUOTLF>2.0.CO;2

Pritchard, M., & Huntley, D. A. (2006). A simplified energy and mixing budget for a small river plume discharge. *Journal of Geophysical Research: Oceans*, *111*, 1–11. https://doi.org/10.1029/2005jc002984

Ralston, D. K., Cowles, G. W., Geyer, W. R., & Holleman, R. C. (2017). Turbulent and numerical mixing in a salt wedge estuary: Dependence on grid resolution, bottom roughness, and turbulence closure. *Journal of Geophysical Research: Oceans*, *122*, 692–712. https://doi.org/10.1002/2016jc011738

Rijnsburger, S., Flores, R. P., Pietrzak, J. D., Horner-devine, A. R., & Souza, A. J. (2018a). The influence of tide and wind on the propagation of fronts in a shallow river plume. *Journal of Geophysical Research: Oceans*, *123*, 1–17. https://doi.org/10.1029/2017jc013422

Rijnsburger, S., Flores, R. P., Pietrzak, J. D., Horner-Devine, A. R., Souza, A. J., & Zijl, F. (2021). Numerical model data underlying the publication: The evolution of plume fronts in the Rhine region of freshwater influence. TU Delft. https://doi.org/10.4121/13664471

Rijnsburger, S., Flores, R. P., Pietrzak, J., Horner-Devine, A. R, & Souza, A. J (2018b). *Frontal periods*. TU Delft. https://doi.org/10.4121/uuid:5d0c5be2-8294-4e05-a859-7968cfd9bac1

Rijnsburger, S., van der Hout, C. M., van Tongeren, O., de Boer, G. J., van Prooijen, B. C., Borst, W. G., & Pietrzak, J. D. (2016). Simultaneous measurements of tidal straining and advection at two parallel transects far downstream in the Rhine ROFI. *Ocean Dynamics*, *66*, 719–736. https://doi.org/10.1007/s10236-016-0947-x

Shin, J. O., Dalziel, S. B., & Linden, P. F. (2004). Gravity currents produced by lock exchange. *Journal of Fluid Mechanics*, *521*, 1–34. https://doi.org/10.1017/s002211200400165x

Signell, R. P., & Geyer, W. R. (1991). Transient eddy formation around headlands. *Journal of Geophysical Research: Oceans*, *96*, 2561–2575. https://doi.org/10.1029/90jc02029

Simpson, J. H., & Bowers, D. (1981). Models of stratification and frontal movement in shelf seas. *Deep-Sea Research*, *28*, 727–738. https://doi.org/10.1016/0198-0149(81)90132-1

Simpson, J. H., Bos, W. G., Schirmer, F., Souza, A. J., Rippeth, T. P., Jones, S. E., & Hydes, D. (1993). Periodic stratification in the Rhine ROFI in the North Sea. *Oceanologica Acta*, *16*, 23–32.

Simpson, J. H., Brown, J., Matthews, J., & Allen, G. (1990). Tidal straining, density currents, and stirring in the control of estuarine stratification. *Estuaries*, *13*, 125–132. https://doi.org/10.2307/1351581

Simpson, J. H., & Souza, A. J. (1995). Semidiurnal switching of stratification in the region of the Rhine. *Journal of Geophysical Research*, *100*, 7037–7044. https://doi.org/10.1029/95jc00067

Stelling, G. S., & van Kester, J. A. M. (1994). On the approximation of horizontal gradients in sigma coordinates for bathymetry with steep bottom slopes. *International Journal for Numerical Methods in Fluids*, *18*, 915–935. https://doi.org/10.1002/fld.1650181003

Suijlen, J., & Duin, R. D. (2002). Atlas of near-surface total suspended matter concentrations in the Dutch coastal zone of the north sea (*Tech. Rep. No. December*). National Institute for Coastal and Marine Management.

van Alphen, J., de Ruijter, W. P. M., & Borst, J. C. (1988). Outflow and three-dimensional spreading of Rhine river water in the Netherlands coastal zone. In J. Dronkers, & W. van Leussen (Eds.), *Physical processes in estuaries* (pp. 70–92). Berlin. Springer-Verlag. https://doi.org/10.1007/978-3-642-73691-9_5

Verboom, G., de Ronde, J., & van Dijk, R. (1992). A fine grid tidal flow and storm surge model of the North Sea. *Continental Shelf Research*, *12*, 213–233. https://doi.org/10.1016/0278-4343(92)90030-n

Verlaan, M., Zuderveld, A., de Vries, H., & Kroos, J. (2005). Operational storm surge forecasting in the Netherlands: Developments in the last decade. *Philosophical Transactions of the Royal Society A: Mathematical, Physical and Engineering Sciences*, *363*, 1441–1453. https://doi.org/10.1098/rsta.2005.1578

Visser, A. W., Souza, A. J., Hessner, K., & Simpson, J. H. (1994). The effect of stratification on tidal current profiles in a region of freshwater influence. *Oceanologica Acta*, *17*, 369–381.

Yuan, Y., & Horner-Devine, A. R. (2017). Experimental investigation of large-scale vortices in a freely spreading gravity current. *Physics of Fluids*, *29*. https://doi.org/10.1063/1.5006176